Experimental Thermal and Fluid Science 177 (2026) 111782

Contents lists available at ScienceDirect

Experimental Thermal and Fluid Science

journal homepage: www.elsevier.com/locate/etfs

Multi-scale analysis of air–water properties and free-surface dynamics in dam-break waves

D. Regout *, A. van Niekerk, D. Wüthrich

Department of Hydraulic Engineering, Delft University of Technology, Stevinweg 1, Delft, 2628 CN, The Netherlands

ARTICLE INFO

Keywords:
Scale effects
Multi-phase flows
Physical modeling
Dam-break waves
Breaking roller
Highly unsteady flows

ABSTRACT

Aeration plays a key role in the breaking roller of dam-break waves, however, their multiphase behavior remains insufficiently understood due to the complexity of turbulent air–water interactions in unsteady aerated flows. Laboratory experiments are typically designed under Froude similitude to preserve the balance between inertial and gravitational forces. In aerated free-surface flows, incomplete dynamic similarity leads to scale effects as viscous and surface tension forces become increasingly influential at smaller scales. While scaling behavior has been extensively investigated for steady aerated flows, corresponding insights for unsteady flows remain scarce. This study experimentally investigates the scaling behavior of unsteady dam-break wave rollers using geometrically similar experiments at two different scales, each with four flow conditions. A comprehensive dataset was obtained combining free-surface measurements, video-based analysis, and intrusive phase-detection probes, enabling detailed characterization of free-surface dynamics and air–water flow properties. Fluctuations of the roller-toe perimeter agree well between scales, suggesting Froude-dependence. In contrast, free-surface fluctuations along the roller exhibit scale dependence, reflecting the influence of aeration and large recirculating structures. Bubble characteristics showed strong scale effects, underscoring the role of turbulence dissipation and interfacial forces that are not dynamically similar across scales, whereas void-fraction profiles are comparatively less sensitive. Overall, the results demonstrate that many multiphase flow properties cannot be directly extrapolated solely based on Froude similarity. While highlighting the need for prototype measurements, this study provides new insight for improving the extrapolation of laboratory-scale findings to natural unsteady phenomena.

1. Introduction

Long-period waves such as tsunamis, impulse waves, storm surges, and flash floods, pose significant hazards to coastal and riverine regions, and are characterized by highly unsteady free-surface flows. Due to their rare, violent, and unpredictable nature, investigations are typically limited to laboratory experiments conducted at reduced scales, where dam-break waves are commonly used to study (unsteady) shallow-water hydrodynamics [e.g., 1]. A dam-break wave is a gravity-driven positive surge generated by the sudden release of a large volume of water. The resulting abrupt water-level discontinuity induces wave breaking, forming a breaking roller propagating in shallow water. This roller is characterized by intense recirculation and substantial air entrainment, continuously reinforced by strong gradients in water levels, velocities, and pressures at the wavefront [2]. The presence of entrained air significantly modifies the hydrodynamic behavior of the flow, with previous studies highlighting the important role of aeration in surge-wave impacts and wave–structure interactions, where multiphase compressibility effects influence peak pressure magnitudes, impact duration, and pressure oscillations [3–5]. These processes are therefore relevant to a broad range of engineering applications, including the assessment of wave-induced loads on coastal and hydraulic structures, green-water loading on ships, and the validation of numerical models [e.g., 6–8]. Despite its relevance, the multiphase nature of the breaking roller remains poorly understood due to the complexity of turbulent air–water interactions and challenges associated with scaling unsteady multiphase flows. Laboratory experiments are typically designed under Froude similitude to preserve the governing balance between inertial and gravitational forces [9]. However, in reduced-scale multiphase flows, viscous and surface tension effects become increasingly influential as these processes cannot be scaled simultaneously, leading to distortions in air–water dynamics, including air entrainment and bubble break-up processes [10]. Consequently, aerated free-surface flows in down-scaled models are inherently affected by scale effects,

* Corresponding author.
E-mail address: d.regout@tudelft.nl (D. Regout).

https://doi.org/10.1016/j.expthermflusci.2026.111782
Received 19 February 2026; Received in revised form 24 May 2026; Accepted 31 May 2026
Available online 4 June 2026

particularly in their multiphase characteristics. This also affects the up-scaling of laboratory results to prototype applications.

Previous experimental studies on scale effects in aerated flows focused predominantly on steady flow conditions, including stepped spillways [e.g., 11,12] and hydraulic jumps [e.g., 13–16]. For hydraulic jumps scaled under Froude similitude, the global free-surface geometry exhibits self-similar profiles and consistent conjugate depth ratios. Moreover, macroscopic air–water flow properties, including interfacial velocities and void fraction distributions, were observed to be largely unaffected by scale, with only limited effects reported for void fraction distributions at Re< $2.7{\cdot}10^4$ - $6.3{\cdot}10^4$, depending on the Froude number [17,18]. Similar scale-independent behavior was also observed in stepped spillways [19]. In contrast, pronounced scale effects were consistently observed for bubble characteristics, including bubble count rate, bubble chord time, and clustering behavior. At low Reynolds numbers, fewer but larger bubbles were reported, accompanied by reduced turbulence intensities and enlarged turbulent length and time scales, highlighting a strong coupling between turbulence, air entrainment, and bubble break-up processes [14,19]. Felder and Chanson [12] further investigated scaling effects on air–water flow properties in two geometrically scaled stepped spillways by comparing Froude and Reynolds similitude. Although Reynolds similitude provided a marginal improvement in the scaling of bubble chord sizes relative to Froude similitude, neither approach was sufficient to fully eliminate scale effects on microscopic air–water flow properties. This highlights the intertwined influences of gravitational, inertial, viscous, and surface tension forces in strongly aerated flows, showing that while global flow features may scale satisfactorily, air–water interactions are not adequately preserved under Froude similitude.

Multiphase behavior in unsteady flows has been analyzed by Leng and Chanson [20], Shi et al. [21], and Regout et al. [2], however, these studies were all conducted at a single scale. While dam-break waves and breaking bores are often considered analogous to translating hydraulic jumps [e.g., 22–24], this comparison is constrained by differences in inflow conditions and flow patterns. Consequently, the scaling of air–water flow properties in unsteady flows remains largely unexplored.

In this context, the present study provides novel experimental insights into the scaling behavior of unsteady dam-break wave rollers. Geometrically similar experiments were conducted at two different scales, enabling direct comparison of flow conditions with identical Froude numbers but differing Reynolds numbers. Building on the single-scale experiments by Regout et al. [2], this study extends the previous investigation, focusing on free-surface dynamics and detailed air–water characteristics in unsteady flows at various scales. Overall, these findings contribute to a more reliable interpretation of multiphase free-surface flow experiments, supporting the extrapolation of laboratory results to natural phenomena at the prototype scale.

2. Experimental approach

The experiments at the two scales were conducted during two separate experimental campaigns. Measurements from the large-flume experiments, including Acoustic Displacement Meters (ADM) and conductivity probes, were previously analyzed by Regout et al. [2]. In addition, reference probe data from two flow conditions of the small-flume experiments were used to perform a complementary sensitivity analysis of the threshold value in the single-threshold technique (see Section 3.2) [25]. Building on this prior work, the present study extends the analysis to a multi-scale investigation of dam-break wave dynamics by integrating the large-flume probe dataset of [2] with the newly analyzed small-flume dataset and high-speed top-view imaging.

2.1. Experimental set-up

Two similar sets of experiments were conducted at the Hydraulic Engineering Laboratory of Delft University of Technology, the Netherlands, where dam-break waves were generated in two horizontal flumes of proportional scale. The small-flume experiments were performed in a flume 14 m long, 0.40 m wide, and 0.42 m deep, with a glass bottom. The large-flume experiments were conducted in a flume 39 m long, 0.76 m wide, and 0.85 m deep, with a smooth concrete bed. In both set-ups, a lift gate was used to enforce a sudden opening, generating a dam-break wave over a still water level h_0. The roller toe is defined as the initial transition from the still water level to the resulting breaking roller, which propagates downstream with celerity U, followed by a quasi-uniform depth referred to as the plateau height h_p (Fig. 1a). To ensure that the gate opening did not affect the wave properties, the opening time of both gates satisfied the criterion of [26], $t < \sqrt{2d_0/g}$, where d_0 is the reservoir impoundment depth.

2.2. Dimensional analysis

Key flow characteristics include free-surface features and air–water properties defined as functions of time, space, and vary with initial conditions. The unsteady nature of the flow restricts measurements to an Eulerian reference system, resulting in data acquired in the temporal domain and expressed in dimensionless form as $t^* = t\sqrt{g/d_0}$. The spatial coordinates y, z are non-dimensionalized as $y^* = y/W$ (where W is the flume width) and $z^* = (z - h_0)/(h_p - h_0)$.

The dominant mechanisms in multiphase flows are characterized by Froude, Reynolds, and Weber numbers. The Froude number, $\mathrm{Fr}=U/\sqrt{gh_0}$, is the primary similarity parameter for preserving inertial-gravitational force balance in reproducing gravity-driven free-surface flows at laboratory scale [9]. The Reynolds number, $\mathrm{Re} = (\rho U h_0)/\mu$, characterizes viscous and turbulent effects, while the Weber number, $\mathrm{We}=(\rho h_0 U^2)/\sigma_s$, quantifies the influence of surface tension, where ρ is the water density, μ the dynamic viscosity, and σ_s the surface tension. The Froude, Reynolds and Weber number are related through the Morton number, $\mathrm{Mo}= g\mu^4/(\rho\sigma_s^3)=\mathrm{We}^3/(\mathrm{Fr}^2\mathrm{Re}^4)$, which remains constant for a given fluid [27]. For geometrically similar models using identical fluids, Froude similitude implies lower Reynolds and higher Weber numbers compared to prototype conditions, inducing scale effects associated with viscous and surface tension forces. Under Morton similarity, this yields $\mathrm{We} \propto \mathrm{Re}^{4/3}$, consequently, scaling effects are quantified in terms of Froude and Reynolds numbers.

2.3. Instrumentation

Free-surface elevations were measured using microsonic mic+35/IU/TC Acoustic Displacement Meters (ADM) with a response time < 64 ms and precision ±0.1 mm. In each set-up, 3 ADMs were installed along the centerline at x/d_0 = 11.7, 14.2, 16.7 (Fig. 1a).

Top-view recordings were obtained to detect the fluctuating behavior of the propagating wavefronts. For each flow condition (FC) in both flumes, 25 videos were recorded using a Photron FASTCAM NOVA S16 ultra-high-speed camera equipped with a NIKKOR Z 50 mm f/1.4 lens, capturing images at a resolution of 1024 × 1024 pixels and 16,000 frames per second (fps). The camera was positioned at x/d_0=15.9 downstream of the gate at elevations z_{vc}/d_0=2.9 and 2.7 in the small and large flume, respectively (Fig. 1a), yielding fields of view (FOV) of 44 × 44 cm and 78 × 78 cm. The exposure time was set to 2 μs, with the camera focused on the surface of the initial water level h_0. LED arrays were installed downstream of the camera and oriented toward the incoming wavefront to provide uniform illumination. A black flume bed and black cloth covering the experimental set-up were used to enhance image contrast and suppress reflections.

Air–water flow properties were obtained using four double-tip phase-detection conductivity probes located at x/d_0=17.6 downstream

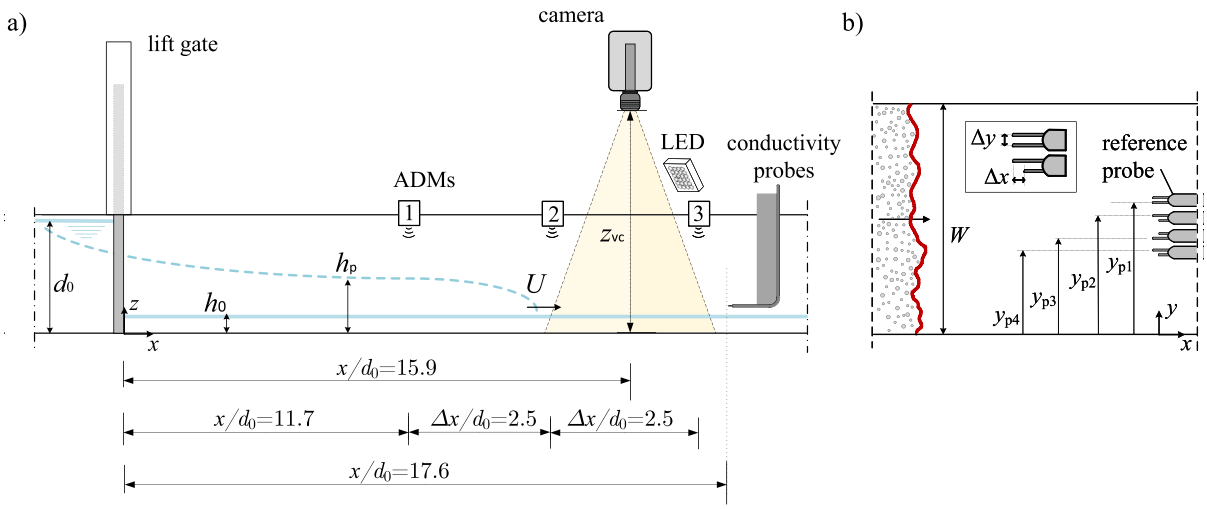

Fig. 1. Experimental set-up: (a) side-view sketch with reservoir depth d_0=0.4 m (small flume) and d_0=0.8 m (large flume), and (b) top-view sketch of the phase-detection probes with flume widths W=0.4 m (small flume) and W=0.78 m (large flume). The roller-toe perimeter is indicated in red.

Table 1
Characteristics of the tested flow conditions (FC).

Flume	Flow condition	d_0 [m]	h_0 [m]	$\frac{h_0}{d_0}$	h_p [m]	U [m/s]	Fr	Re	We
small flume (SF)	FC1	0.4	0.016	0.04	0.11	2.09	5.27	$0.33{\cdot}10^5$	$0.99{\cdot}10^3$
	FC2	0.4	0.032	0.08	0.14	1.97	3.52	$0.63{\cdot}10^5$	$1.77{\cdot}10^3$
	FC3	0.4	0.048	0.12	0.16	1.97	2.87	$0.95{\cdot}10^5$	$2.66{\cdot}10^3$
	FC4	0.4	0.064	0.16	0.18	1.95	2.46	$1.25{\cdot}10^5$	$3.48{\cdot}10^3$
large flume (LF)	FC1	0.8	0.032	0.04	0.22	2.88	5.14	$0.92{\cdot}10^5$	$0.38{\cdot}10^4$
	FC2	0.8	0.064	0.08	0.29	2.82	3.56	$1.80{\cdot}10^5$	$0.73{\cdot}10^4$
	FC3	0.8	0.096	0.12	0.33	2.75	2.83	$2.63{\cdot}10^5$	$1.04{\cdot}10^4$
	FC4	0.8	0.128	0.16	0.37	2.73	2.44	$3.49{\cdot}10^5$	$1.36{\cdot}10^4$

Note that: $\mathrm{Fr}=U/\sqrt{gh_0}$, $\mathrm{Re}=\rho U h_0/\mu$, and $\mathrm{We}=\rho h_0 U^2/\sigma_s$, using water density $\rho = 1000\,\mathrm{kg\,m^{-3}}$, dynamic viscosity $\mu = 1.002\cdot10^{-3}\,\mathrm{Pa\,s}$, and surface tension $\sigma_s = 0.07\,\mathrm{kg\,s^{-2}}$. U and h_p are obtained from the ADM measurements.

of the gate. The probes were sampled simultaneously at 100 kHz, and horizontally aligned at $y_{p,i}/W$=[0.35, 0.42, 0.54, 0.62] in the small flume and $y_{p,i}/W$=[0.31, 0.35, 0.46, 0.56] in the large flume (Fig. 1b). Each probe tip had an inner electrode with $\varnothing$ = 0.25 mm, where the reference probe featured two leading tips (Δx = 0 mm), while the remaining three probes had a longitudinal tip spacing of Δx = 6.3 mm. The reference probe remained fixed at h_0+5 mm and h_0+3 mm in the large and small flume, respectively, to ensure synchronization across all tests. The remaining three probes were positioned at varying elevations and adjusted across four configurations, covering 13 elevations ranging from slightly below the initial water level to the plateau height. Each configuration consisted of 55 repetitions per elevation to allow for ensemble-average analysis, yielding a total of 220 repetitions recorded by the reference probe for each FC. Further details on the probe set-up are provided in [2].

2.4. Flow conditions

For all tests, the impoundment depth d_0 remained constant, while different flow conditions were obtained by varying the downstream water level h_0, as summarized in Table 1.

3. Methodology and data processing

The unsteady nature of the flow restricts data acquisition to an Eulerian reference frame, limiting measurements to short durations. Consequently, data analysis requires ensemble-averaging approach, based on sufficient number of repetitions [28].

3.1. Ensemble analysis of ADM measurements

Free-surface levels were measured using ADMs, resulting in 220 profiles per flow condition (FC) at each scale. Raw voltage signals V were converted to distances using calibration functions and then filtered using a Z-score filter to remove far-range noise, followed by a third-order Savitzky–Golay (SG) filter to attenuate small outliers [29]. Repetitions were synchronized by setting t = 0 at wave arrival at each ADM. Ensemble-averaged free-surface profiles were computed for each FC. Wavefront celerity was obtained as $U = \Delta x/\Delta t$, where Δx and Δt denote the distance and travel time between adjacent ADMs.

3.2. Ensemble analysis of phase-detection probe data

Air–water flow properties are derived from phase-detection probe measurements. The signal processing and the definitions of the parameters follow the methodology used by Regout et al. [2]. This framework is adopted here to ensure methodological consistency between previously study and the new small-flume measurements.

As the wavefront propagates through the probes, the two phases are detected based on conductivity differences, visualized as a drop in voltage in the raw signal when the probe tip is exposed to air (Fig. 2). Each raw signal V was first normalized using V_{max} and V_{min} from its bimodal distribution and then binarized using a single-threshold technique [30] to obtain the instantaneous void fraction c. To this end, a threshold value of 0.5 is commonly used for steady flows [e.g., 15,31–33]; however, unsteady flow conditions can lead to more incomplete piercings [34,35]. Based on a sensitivity analysis by Wüthrich and

Regout [25], a higher threshold value of 0.8 was therefore adopted to effectively capture smaller bubbles in unsteady flows, such that:

$$c(z,t) = \begin{cases} 0\,(\text{water}) & \text{if} \quad (V(t) - V_{\min})/(V_{\max} - V_{\min}) > 0.8 \\ 1\,(\text{air}) & \text{if} \quad (V(t) - V_{\min})/(V_{\max} - V_{\min}) \leq 0.8 \end{cases}$$

The instantaneous void fraction c provides information on the number of air–water and water–air interfaces, their temporal distribution, and the duration between successive transitions at each elevation (Fig. 2). For each FC, all repetitions were synchronized using the first air–water interface detected by the right tip of the reference probe. Ensemble-averaged statistical analyses were applied across n repetitions at each elevation ($n = 55$, except at the reference probe elevation where $n = 220$) to obtain characteristic air–water flow parameters, in line with previous studies by Leng and Chanson [20], Wüthrich et al. [28], and Regout et al. [2].

The number of interfaces N is obtained from the binarized signal, with an interface defined as a transition between air and water (or vise versa). These transitions correspond to the boundaries of intercepted air bubbles and water droplets, such that N is related to the bubble content within the roller. For measurements at elevations above the initial water level h_0, the probes are initially in air and the first detected transition is from air to water. The number of detected bubbles is therefore given by $b = (N-1)/2$ for $z > h_0$, while $b = N/2$ for $z < h_0$ since the tip is initially located in water.

As shown in Fig. 2, the bubble chord time t_{ch} is defined as the time between consecutive water–air and air–water interfaces. Based on t_{ch} and wavefront celerity U, a characteristic pseudo bubble length scale L_{ch} is defined as:

$$L_{ch} = U t_{ch}, \tag{1}$$

which corresponds to its maximum pseudo-chord length when the probe pierces the bubble near its center.

Finally, the ensemble-averaged void fraction C is defined following [20,28] as:

$$C(z,t) = \frac{1}{n}\sum_{j=1}^{n} c_j(z,t) \tag{2}$$

where the instantaneous void fraction c_j is considered a Bernoulli variable (1 = air, 0 = water), and n is the number of repetitions at each elevation. Consequently, the void fraction profiles $C(z,t)$ represent the probability of air presence within the roller. The depth-averaged void fraction $C_{mean}(t)$ was computed by integrating each vertical distribution between $z = 0$ and $z = z_{90}$:

$$C_{mean}(t) = \frac{1}{z_{90}}\int_0^{z_{90}} C(z,t)\mathrm{d}z \tag{3}$$

where z_{90} is the elevation where $C(z,t) = 0.9$, commonly adopted to characterize the free-surface level in air–water flows.

3.3. Image analysis of top-view videos

As the wave passed through the camera's field of view (FOV), brightness variations created visible contrast between the initial water level and the advancing wavefront. These resulting pixel-intensity gradients in the grayscale images were used to identify the roller-toe perimeter (Fig. 1b). In line with [36], the image-based analysis consisted of three steps: (1) image processing to detect the roller-toe perimeter in each frame, (2) filtering the perimeters to remove noise and droplet ejection, and (3) obtaining roller characteristics. A schematic overview of the workflow, illustrating the different processing steps, is shown in Fig. 3.

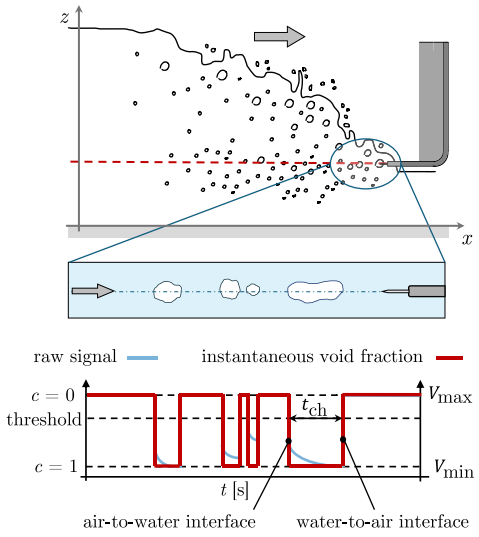

Fig. 2. Sketch of signal processing captured by a probe tip, using single threshold technique, set at 80%.

3.3.1. Step 1: image processing

For each flume, 25 videos were recorded per FC. The videos were decomposed into individual frames, to which identical image-processing techniques were applied to detect the roller-toe perimeter. The videos were pre-processed to enhance image quality, including high dynamic range (HDR), gamma, contrast, and brightness adjustments, where these parameters were manually optimized. All videos, originally recorded at 16,000 fps, were downsampled to 3200 fps, with the duration defined by the first and last frames where the top-view profile was fully visible across the flume width. Fig. 3 illustrates the step-by-step image processing procedure. Each frame was first cropped vertically to remove sidewall reflections, yielding an effective cross-sectional width of W'=868 and 899 pixels for the small and large flume, respectively. The cropped grayscale images were then binarized using a threshold $p_{i,thres} = 20$, setting pixels to 0 (black) for $p_i \leq p_{i,thres}$ and 255 (white) otherwise. A 5 × 5 median filter was then applied to reduce impulse noise. Finally, the roller perimeter was detected via gradient-based edge detection, with the roller toe defined as the first non-zero pixel from the right.

3.3.2. Step 2: data filtering

Strong fluctuations and air entrainment at the roller toe generate transient foamy structures, droplets, and splashes, causing detected edges to include local ejections and noise. Therefore, the perimeters extracted from each frame were filtered using a two-step procedure (Fig. 3). A Z-score filter ($Z_{thres} = 2.8$) and a second-order Savitzky–Golay (SG) filter were applied to remove far-range noise and small outliers near the roller-toe boundary, respectively, with outliers replaced by linear interpolation. The window length of the SG filter and threshold values were scale-dependent and selected by trial and error to balance noise reduction and boundary fidelity. For the small flume, a window length of 19 pixels and a threshold of 10 pixels were used, while for the large flume these values were 49 and 15 pixels, respectively.

3.3.3. Step 3: roller-toe characteristics

Analyzed characteristics include the median roller-toe position, roller-toe fluctuations, wavefront celerity, instantaneous roller-toe celerity, and indentation coefficient (Fig. 3). For each frame i, the median roller-toe position $x_{med,i}$ was determined across the flume width. Roller-toe fluctuations in each frame i were defined as the longitudinal deviations from the median position, $x'_{i,j} = x_{i,j} - x_{med,i}$, where $x_{i,j}$ is the roller-toe position at pixel j in the transverse (y) direction and $x_{med,i}$

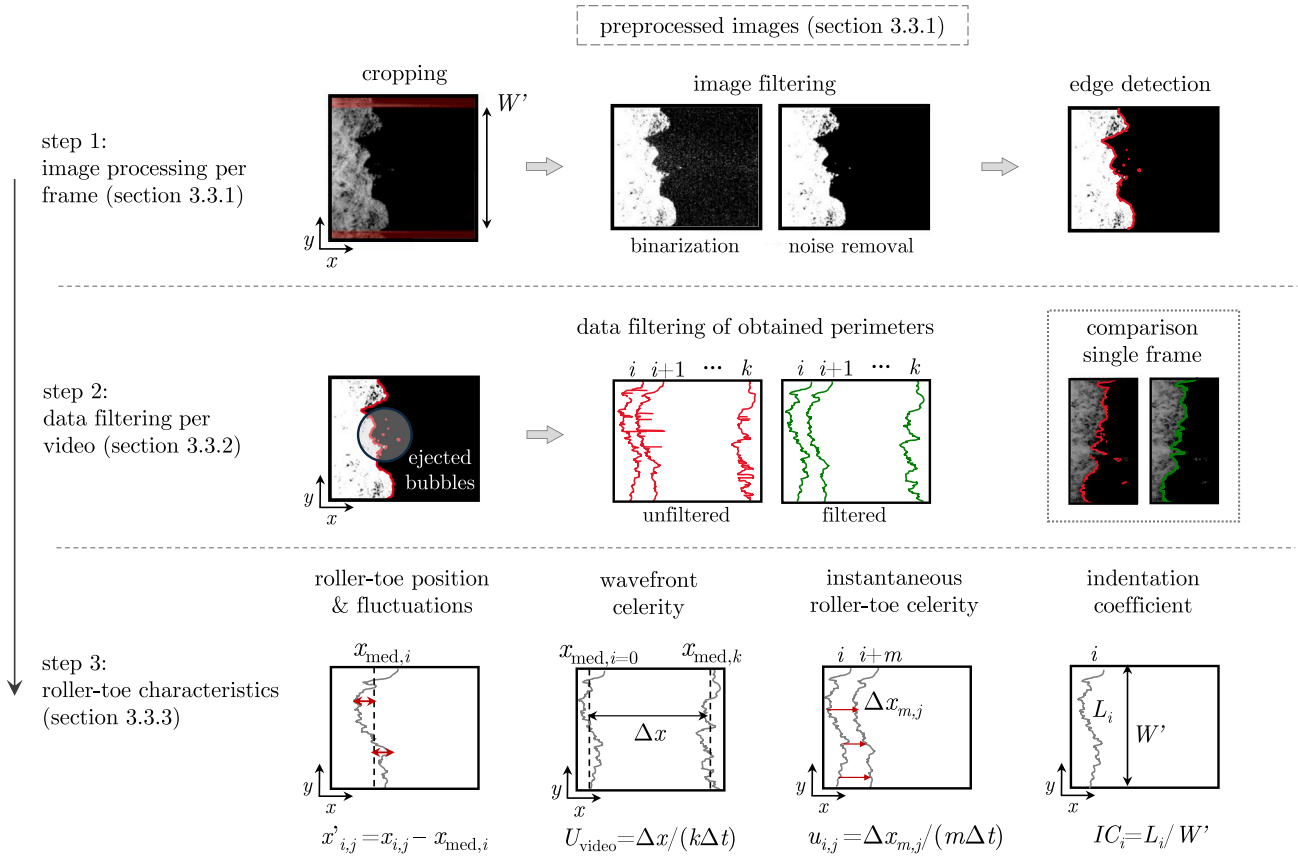

Fig. 3. Schematic of the image-processing workflow to obtain roller-toe characteristics, based on 25 videos per FC. The wave propagates from left to right.

is the median roller-toe position. The fluctuations x' are computed for each wave profile across all transverse pixels and for all 25 videos per FC.

For each video, the wavefront celerity is defined as $U_{\text{video}} = \Delta x/(k\Delta t)$, where Δx is the distance traveled by the median roller-toe position x_{med} between the first and last frames, Δt is the time between consecutive frames (corresponding to 1/3200 s), and k is the total number of frames in the video. Accordingly, the ensemble-averaged wavefront celerity is obtained from 25 videos for each FC.

The wavefront exhibits a local celerity that varies in space and time, referred to as the instantaneous roller-toe celerity u. When computed between two consecutive frames (Δt = 1/3200 s), the temporal resolution resulted in unrealistically small estimates. Therefore, u in each frame i was evaluated over a finite interval of m frames and defined as $u_{i,j} = \Delta x_{m,j}/(m\Delta t)$, where $\Delta x_{m,j}$ is the displacement between frames i and $i+m$ along vertical pixel j. Based on a sensitivity analysis, m was set to 28 for the small flume and (consistent with Froude scaling) to 40 for the large flume, resulting in accuracies of 0.05 and 0.06 m/s, respectively. The instantaneous celerities u were computed for each wave profile across all transverse pixels and for all 25 videos per FC.

Lastly, the indentation coefficient quantifies fluctuation magnitude as the ratio of perimeter length to flume width: $IC_i = L_i/W'$, where IC=1 corresponds to a straight line. The roller-toe perimeter length L_i is determined using the Pythagorean theorem applied to discretized data at pixel resolution, and W' is the effective width of the flume in the cropped image (Fig. 3). IC is computed for each wave profile in all 25 videos per FC.

4. Visual observations

The sudden opening of the gate induces the formation of a dam-break wave with a breaking roller that propagates downstream. The roller consists of a highly aerated strong recirculating flow, sustained by sudden changes in water level, velocity, and pressure at the wavefront. Free-surface instabilities and strong turbulence lead to repeated (de-)aeration processes, producing rapidly evolving and shortly lived foamy structures, droplets, splashes, air cavities, and clusters of bubbles [37]. The recirculating flow near the roller toe continuously entrains air pockets into the wavefront, which are broken into smaller bubbles within the developing shear layer. Side-view observations reveal vortical structures generated by strong shear and associated with Kelvin–Helmholtz instabilities, which are advected downstream together with the entrained bubbles (Fig. 4a). As the roller evolves, these structures gradually dissipate, while the bubbles rise toward the free surface due to buoyancy [20,37]. Similar processes were observed for all flow conditions.

Figs. 4b,c show top-views of breaking rollers in dam-break waves at two scales for Fr = 2.4. In both cases, the flow is characterized by large free-surface deformations and intense air entrainment. The breaking roller in the large flume exhibits significantly greater aeration, visualized by the denser regions of high pixel intensity (white) (Fig. 4c). At larger scale, a wider range of air–water structures is observed, indicating different aeration mechanisms that depend on the relative importance of turbulence and surface tension, as reflected in the Froude, Reynolds, and Weber numbers [37,38]. In contrast, individual bubbles are more clearly distinguishable at the small scale (Fig. 4b). The closer position of the camera in the small-scale experiments provides a higher spatial resolution, allowing finer features to be resolved.

5. Hydrodynamic behavior

The hydrodynamic behavior of dam-break waves is characterized by strong fluctuations along the free surface and the roller toe. The free-surface characteristics are quantified through wave profiles, wavefront

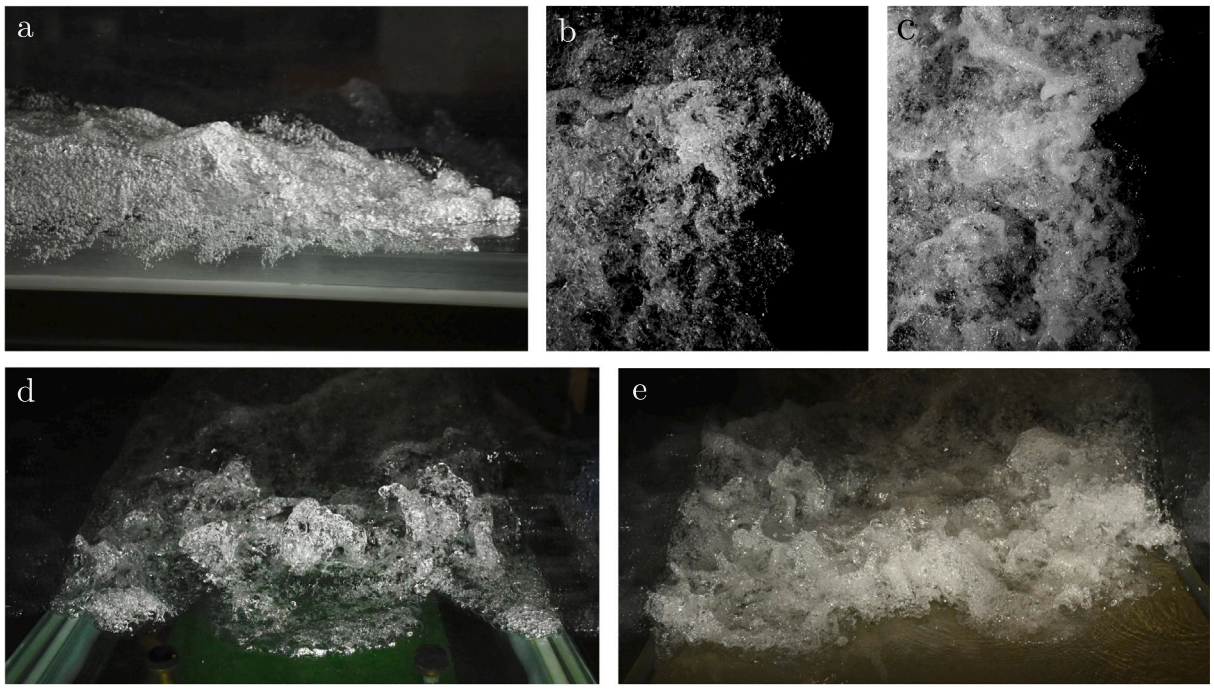

Fig. 4. Visual observations of dam-break waves: (a) side-view of the small flume [Fr = 2.46; Re = 1.25 ·10^5; d_0 = 0.4 m; h_0 = 0.064 m], (b) top-view of FC4$_{SF}$ [Fr = 2.46; Re = 1.25 ·10^5; d_0 = 0.4 m; h_0 = 0.064 m], (c) top-view of FC4$_{LF}$ [Fr = 2.44; Re = 3.49 ·10^5; d_0 = 0.8 m; h_0 = 0.128 m], (d) cross-sectional view of the small flume [Fr = 2.87; Re = 0.95 ·10^5; d_0 = 0.4 m; h_0 = 0.048 m], and (e) cross-sectional view of the large flume [Fr = 2.83; Re = 2.63 ·10^5; d_0 = 0.8 m; h_0 = 0.096 m]. Photos a, d, and e were captured using a DSLR camera (where d and e were published in [25]), while photos b and c were captured using a high-speed video camera (16,000 fps). In photos a–c, the waves propagate from left to right.

celerity, and roller length, while the roller-toe behavior is analyzed in terms of perimeter fluctuations, instantaneous celerity, and indentation coefficient.

5.1. Dynamic behavior of the free surface

Fig. 5a shows the ensemble-median free-surface profiles z_{med} measured by the ADMs, and elevations z_{90} based on the conductivity probe data (Section 3.2). The profiles are normalized using the impoundment depth d_0, and visualized for flow conditions FC1 and FC4 at both scales. Overall, good agreement between both measurement techniques and across scales is observed, with water levels increasing monotonically toward a quasi-uniform depth. The ADMs yield slightly lower free-surface elevations than those obtained with the conductivity probes. These discrepancies can be attributed to differences in instrumentation: the intrusive probes detect elevations corresponding to 90% aeration, whereas the non-intrusive ADMs rely on reflected acoustic signals that penetrate deeper into the aerated region [39]. For all FCs, rapidly evolving fluctuations were observed along the free surface (Fig. 4). These fluctuations were defined as deviations from the ensemble median $z' = z - z_{med}$, based on the ADM data. Fig. 5c presents the interquartile range (IQR) of the normalized fluctuations z'_{IQR}/h_0, showing that the largest fluctuations consistently occur near the roller toe. At both scales, increasing Fr leads to stronger fluctuations, in line with previous studies on hydraulic jumps, attributing this behavior to enhanced air entrainment at the jump toe and air–water projections above the roller [15,31,40]. While Wang [15] reported minimal differences across Reynolds numbers for hydraulic jumps, the large-scale (LF) dam-break waves exhibit significantly larger fluctuations closer to the roller toe ($t\sqrt{g/d_0} < 1.0$), compared to the small-scale tests (Fig. 5c). These scaling effects are likely associated with the higher Reynolds and Weber numbers, which influence (de-)aeration mechanisms and turbulent processes beneath the free surface [36,38].

With increasing distance from the wavefront, both free-surface slope and fluctuations decrease, and the flow approaches a quasi-uniform plateau height, h_p. At both scales, increasing the initial water level h_0 results in higher plateau heights and steeper wavefronts (Fig. 5a), consistent with previous dam-break studies [41, among others]. Fig. 5b shows the median plateau height h_p and wavefront celerity U, derived from both ADM and video data (Section 3), and compares them with analytical predictions by Stoker [42] and Chanson [1]. The measured h_p show excellent agreement with existing formulations across all FCs and scales. Good agreement is also found for U, where small variations between ADM- and video-based celerities can be linked to differences between the two techniques. This is because the video-based estimates are derived over a shorter streamwise distance than the ADM measurements, making them more sensitive to local accelerations and decelerations, whereas ADM-based celerities represent more spatially averaged values. In addition, ADMs provide centerline measurements, while video data capture spatial variability across the flume width. To evaluate potential sidewall effects, Fig. 6 illustrates the variations of U across the flume width W, of FC2, for both scales. The flume width was subdivided into cross-sectional segments, and the mean celerity within each segment was compared with the overall averaged wavefront celerity U. In both flumes, slightly higher celerities were observed near the centerline, indicating weak sidewall effects. This observation was found across all FCs and aligns with previous observations [36,43], however, the influence of sidewall effects appears minimal in the present study. Despite this, the close agreement of h_p and U with the analytical predictions of Stoker [42] confirms that the experimental setup reproduces dam-break wave dynamics, with consistent results across scales indicating that both quantities are preserved under Froude similitude.

The roller length is commonly defined (analogous to hydraulic jumps) as the streamwise distance over which the water elevation increases monotonically [15]. In contrast to earlier studies relying on visual observations, the present study defined the roller length using free-surface fluctuation statistics, $L_r = Ut_{h_p}$, where t_{h_p} is the time needed to reach the plateau height. Fig. 5d presents the roller length normalized by the initial water level h_0, compared with data

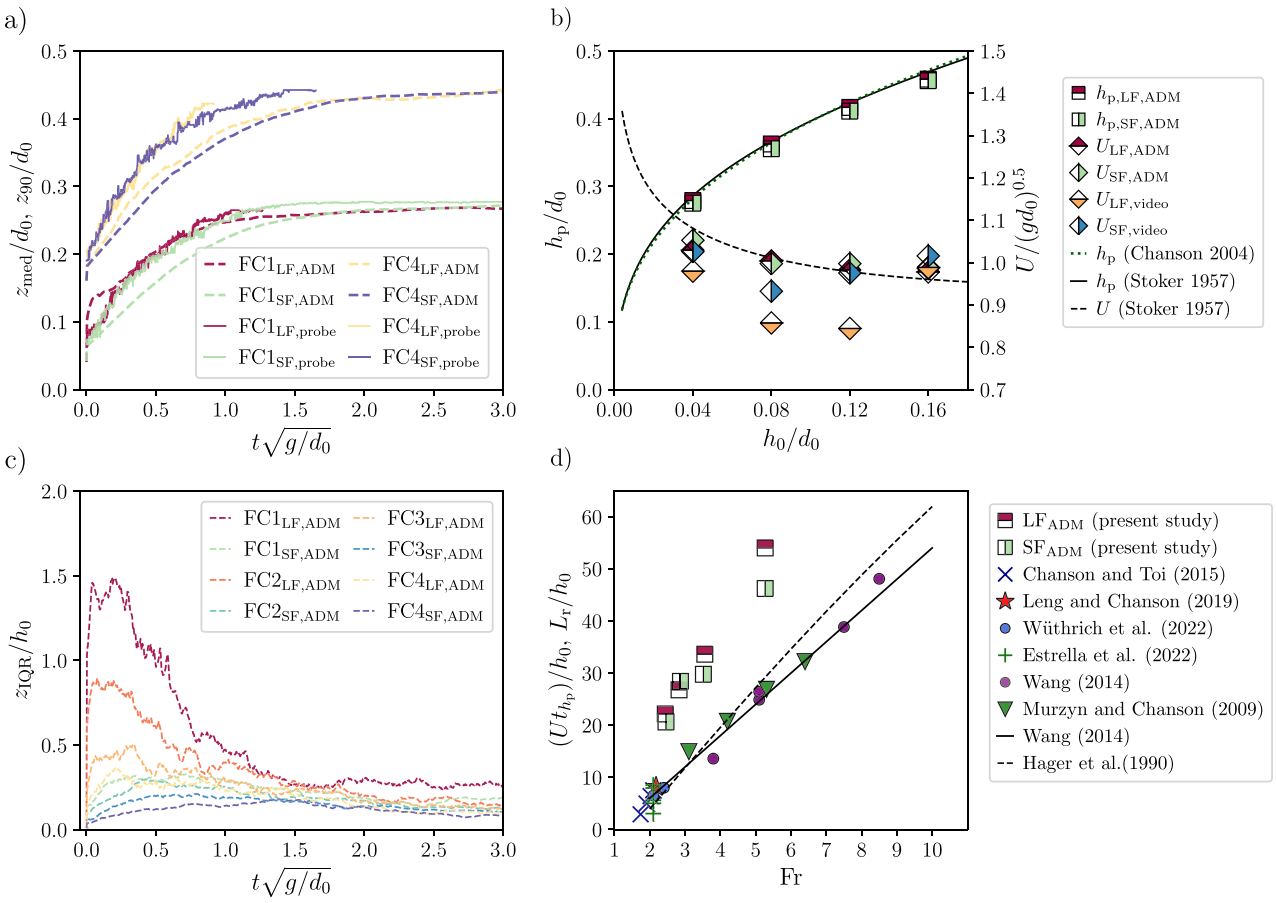

Fig. 5. Free-surface dynamics of dam-break waves at two different scales: (a) Normalized free-surface profiles measured with ADMs (z_{med}) and probe-based elevations (z_{90}) for FC1 (Fr = 5.2) and FC4 (Fr = 2.4) in the large flume (LF, d_0=0.8 m) and small flume (SF, d_0=0.4 m). (b) Normalized wavefront celerity U and plateau height h_p compared with the analytical formulations of Stoker [42] and Chanson [1] for flow conditions FC1–FC4 (Fr = 2.4–5.2) at both scales, with large flume [LF: Re = $0.92{\cdot}10^5$–$3.49{\cdot}10^5$; d_0=0.8 m; h_0=0.032–0.128 m] and small flume [SF: Re = $0.34{\cdot}10^5$–$1.25{\cdot}10^5$; d_0=0.4 m; h_0=0.016–0.064 m]. (c) Normalized free-surface fluctuations quantified by the ADM interquartile range (IQR) for FC1–FC4 at both scales (LF and SF). (d) Normalized roller lengths for FC1–FC4 at both scales, compared with previous studies of breaking bores [20,22,28] and hydraulic jumps [15,16,40,44].

from previous studies on breaking bores and hydraulic jumps. Results show increasing L_r with increasing Fr, consistent with previous studies. However, dam-break waves exhibit slightly larger roller lengths than breaking bores and hydraulic jumps. While Wang [15] and Hager et al. [44] proposed linear relations to estimate L_r as function of Fr, suggesting primarily Froude-based dependence, Estrella et al. [16] also reported a noticeable influence of Re, indicating that the roller length may also depend on Reynolds number. As free-surface fluctuations are larger in the large flume than in the small flume, this affects the estimated roller length, particularly for FC1 (Fr=5.2). Moreover, owing to the higher wavefront celerity, the resulting roller length remains sensitive to its duration t_{h_p}, highlighting the inherent difficulty of defining L_r unambiguously using quantitative criteria.

5.2. Dynamic behavior of the roller toe

The dynamic behavior of the roller toe plays a key role in initiating air entrainment and shear layer development, generating turbulent structures and air–water interactions that influence free-surface dynamics and the aerated roller region. The roller-toe dynamics are based on the top-view video analysis and include roller-toe fluctuations, instantaneous celerity, and indentation coefficient (Section 3.3).

5.2.1. Roller-toe fluctuations

Roller-toe fluctuations are the longitudinal deviation from the median, $x' = x - x_{med}$ (Section 3.3). Fig. 7a compares the probability distributions of roller-toe fluctuations for FC1 and FC4 at both scales, presented in dimensional form and normalized by h_0. For each FC, the fluctuations follow a Gaussian distribution, with the standard deviation σ providing a measure of their magnitude. For similar Froude numbers, dimensional σ is consistently smaller in the small flume (SF) than in the large flume (LF), in line with the larger fluctuations observed in the LF, associated with higher Reynolds numbers (Fig. 4). For different Fr, the distributions in dimensional form are comparable, with a slightly higher σ for FC4 (Fr = 2.4). When normalized, no significant differences are observed between scales, while the influence of the Fr becomes more pronounced.

Fig. 7b presents the normalized standard deviation σ/h_0 as a function of Froude and Reynolds numbers, and compares the results with available data from breaking bores [36] and hydraulic jumps [15,43,45,46]. The standard deviation of roller-toe fluctuations in dam-break waves is consistent with previous studies, exhibiting a linear increase with Fr. Based on the data in 7b, an empirical linear fit is defined as $\sigma/h_0 = 0.34(\mathrm{Fr} - 1)$, valid for $1.5 < \mathrm{Fr} < 6.5$ with $R^2 = 0.84$. Complementarily, σ/h_0 exhibit a slight decrease with increasing Re. These results may suggest that the normalized roller-toe fluctuations are strongly governed by Fr. This prevalence of gravitational processes may be linked to local dynamics at the roller toe, where high-velocity flow impingement and strong shear affect fluctuation dynamics [37,38]. Higher Froude numbers imply steeper velocity gradients between the downstream (still) water and the propagating wavefront tip, generating stronger shear and, consequently, larger horizontal roller-toe

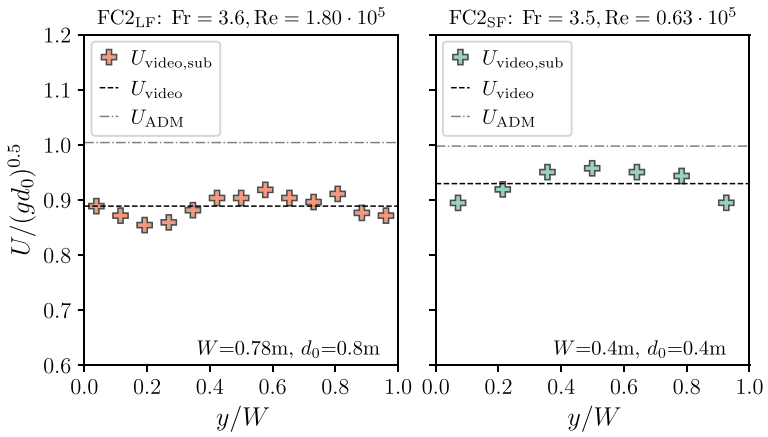

Fig. 6. Normalized averaged wavefront celerity, U, for FC2, evaluated for distinct spatial subsets along the normalized flume width and based on all available video recordings at each experimental scale.

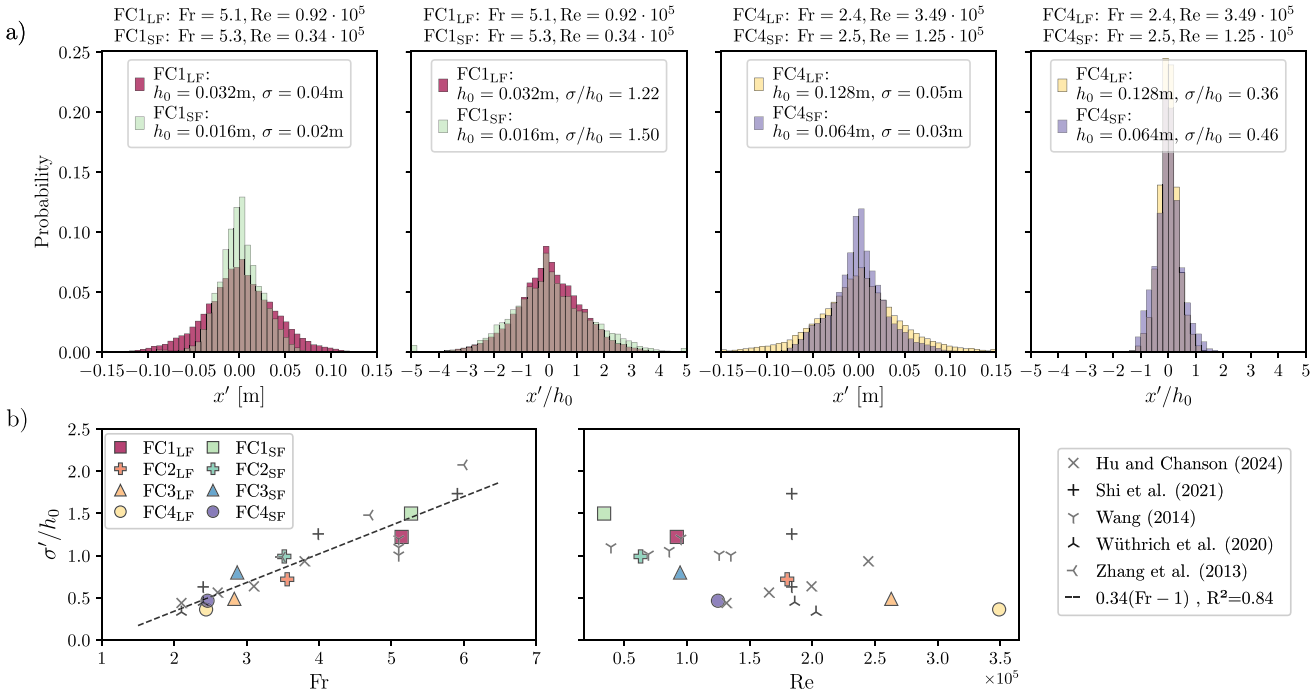

Fig. 7. Roller-toe fluctuations, defined as $x' = x - x_{med}$, at two different scales: (a) Probability distributions of x' for FC1 and FC4 at both scales, shown in dimensional form and normalized by h_0. (b) Normalized standard deviations σ'/h_0 for FC1–FC4 (Fr= 2.4–5.2) at both scales (LF: h_0 = 0.032–0.128 m; SF: h_0 = 0.016–0.064 m), plotted as functions of Froude and Reynolds numbers and compared with previous studies of breaking bores [36] and hydraulic jumps [15,43,45,46].

fluctuations. Bubble dynamics may further contribute to this behavior, since Regout et al. [2] reported an increasing number of bubbles with increasing Fr, particularly slightly above h_0, indicating enhanced air entrainment. Hence, while the largest absolute roller-toe deformations occur at the greatest dimensional length scales (i.e., in the large flume with higher h_0 and Re), the non-dimensional results suggest that the fluctuations are mainly governed by macroscopic, inertia-dominated flow dynamics better described by the Froude number.

5.2.2. *Instantaneous roller-toe celerity*

The instantaneous roller-toe celerity u is defined as the local celerity between successive frames (Section 3.3). Fig. 8 presents the probability distributions of u for FC1 and FC4 in both large and small flumes, shown in dimensional form and normalized with $(gd_0)^{1/2}$. For all FCs, the distributions are negatively skewed, attributed to intermittent local backshifts of the roller toe. Here, the downstream water level effectively acts as a lubricant, causing the roller toe to shift locally upstream relative to the mean propagation and thereby intermittently reducing the instantaneous celerity, where this behavior is consistent with previous findings for breaking bores [36,37]. Notably, fewer negative u values were detected in the present dam-break waves propagating over initially still water, reflecting differences in inflow conditions compared to breaking bores that advance on a flow moving in the opposite direction. The consistently larger IQR in the large flume indicates stronger variations in local roller-toe celerity, while the smaller skewness reflects a higher frequency of low-celerity detections relative to high-celerity ones. Consequently, a slightly lower median is observed for the large flume, explaining the lower wavefront celerity $U_{LF,video}$ in Fig. 5b, and may indicate small scale-effects induced by the larger air entrainment and differences in dissipation mechanisms within the roller. Despite these small differences, the close agreement between normalized u and U across both scales, and with the analytical

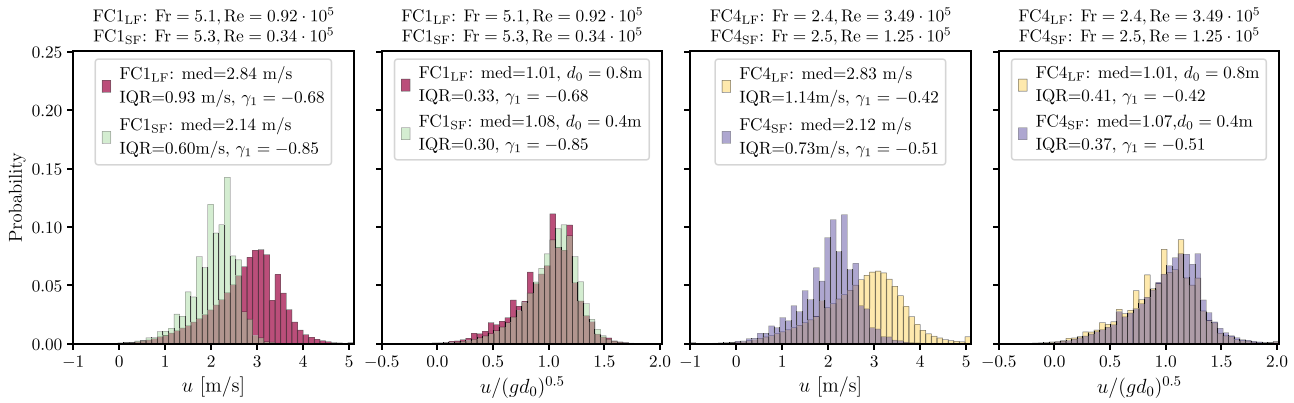

Fig. 8. Probability distributions of the instantaneous roller-toe celerity u (Section 3.3) at both scales, shown in dimensional form and normalized with $(gd_0)^{0.5}$ for FC1 (Fr= 5.2) and FC4 (Fr= 2.4) in the large flume (LF, d_0 = 0.8m) and small flume (SF, d_0 = 0.4m)

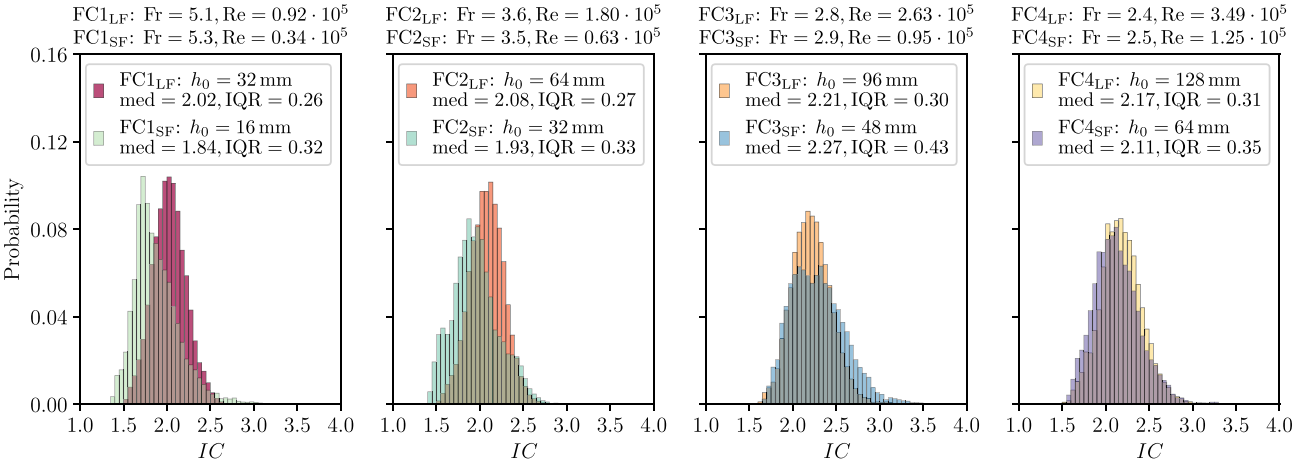

Fig. 9. Probability distributions of indentation coefficient defined as $IC = L/W'$ (Section 3.3) for FC1-FC4 (Fr = 2.4–5.2) at both scales, with the large flume (LF, d_0 = 0.8m) and small flume (SF, d_0 = 0.4m).

formulation by Stoker [42] (Fig. 5b), suggests that roller-toe celerities are primarily governed by Froude-dependent flow dynamics.

5.2.3. Indentation coefficient

The final roller-toe characteristic considered is the indentation coefficient, IC, defined as the ratio of the roller-toe perimeter to the effective channel width (Section 3.3). It quantifies the irregularity of the roller-toe perimeter, such that $IC = L/W' \geq 1$ [36]. Fig. 9 presents the probability distributions of IC for all FCs at both scales. Larger IC values are generally observed under large-scale conditions, reflecting the larger x' found in dimensional form (Fig. 7a). In contrast, the larger IQR in the small flume is consistent with the normalized roller-toe variability, as indicated by the slightly higher σ/h_0 values in Fig. 7b. Overall, the indentation coefficients are comparable to those reported for breaking bores [36]. For similar Fr, dam-break waves show slightly higher median values ($FC4_{LF}$: IC_{med}=2.17, $FC4_{SF}$: IC_{med}=2.11) than breaking bores (Fr = 2.4, IC=1.75), likely reflecting differences in bore generations and inflow conditions.

6. Aerated region in the breaking roller

Visual observations revealed substantial air entrainment and entrapment at the wavefront (Fig. 4). These properties were measured using phase-detection probes and quantified in both flumes using ensemble-averaged statistics of bubble characteristics (number and size) and void fraction (Section 3.2).

6.1. Bubble characteristics

An interface is defined as a phase change detected by the probe tip and corresponds to a transition between water and air (and vice versa). The number of interfaces N provides an indication of the amount of bubbles distributed across the roller (Section 3.2).

Fig. 10a shows the median number of interfaces $\langle N \rangle$ as a function of the normalized elevation z^* for all flow conditions (FCs) at both scales. For all FCs, $\langle N \rangle$ increases for $z^* > -0.05$ to reach a local maximum, then decreases at higher elevations, and finally increases again near the free surface, forming a characteristic S-shaped vertical profile, which is most pronounced at higher Fr in the large flume (LF). The local maximum consistently occurs at $z^* \approx 0.13$–0.30, slightly above the initial water level, confirming the presence of a shear layer at both scales. The dam-break waves in the large flume systematically showed higher $\langle N \rangle$ compared to the small flume (SF), with the largest differences observed near the local maximum within the shear layer, particularly for FC1 (Fr=5.2).

Fig. 10b compares the maximum median number of interfaces, $\langle N \rangle_{max}$, across Froude and Reynolds numbers, together with data from previous studies on breaking bores [20,28]. In the large flume, $\langle N \rangle_{max}$ increases with Fr and decreases with Re, whereas it remains nearly constant across all FCs in the small flume. These trends indicate strong scale effects on the number of interfaces, consistent with previous studies of steady-flow phenomena, which reported higher bubble count rates at higher Re for flows with comparable Fr [18,19,47]. The generally lower values of $\langle N \rangle_{max}$ observed for $FC4_{LF}$ and $FC4_{SF}$ compared to

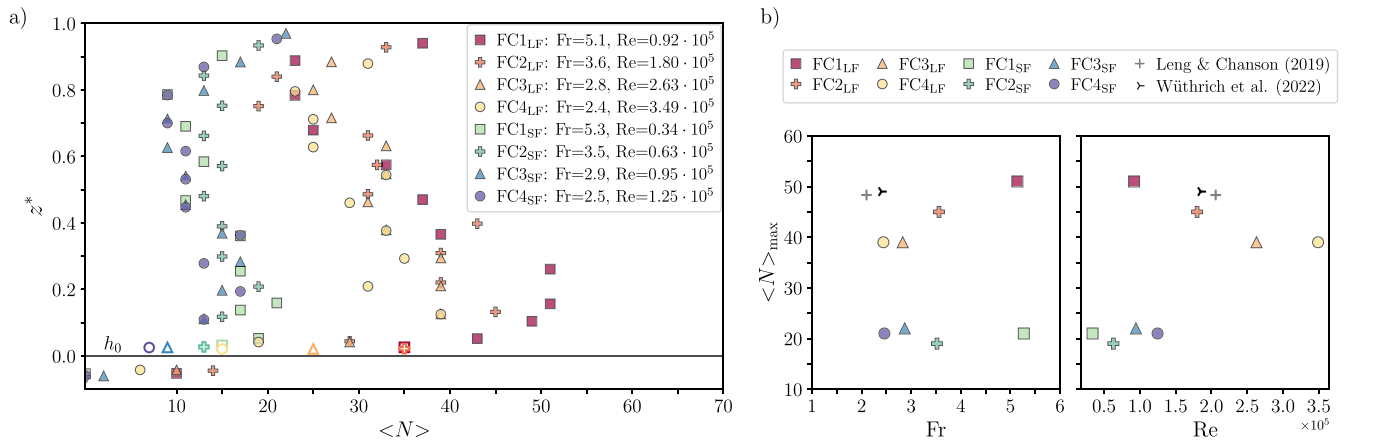

Fig. 10. Ensemble-median number of interfaces $\langle N \rangle$: (a) comparison of $\langle N \rangle$ across normalized elevations z^* for FC1–FC4 (Fr = 2.4–5.2) at both scales with reference probe measurements (based on 220 tests) indicated by open markers, and (b) comparison of $\langle N \rangle_{max}$ plotted against Fr and Re for FC1–FC4 (Fr = 2.4–5.2) at both scales, and compared with breaking bore studies by Wüthrich et al. [28] (Fr = 2.4, Re = 1.86·10^5) and Leng and Chanson [20] (Fr = 2.1, Re = 2.06·10^5), where Fr=$(V_1 + U)/\sqrt{gh_0}$, with V_1 being the initial flow velocity.

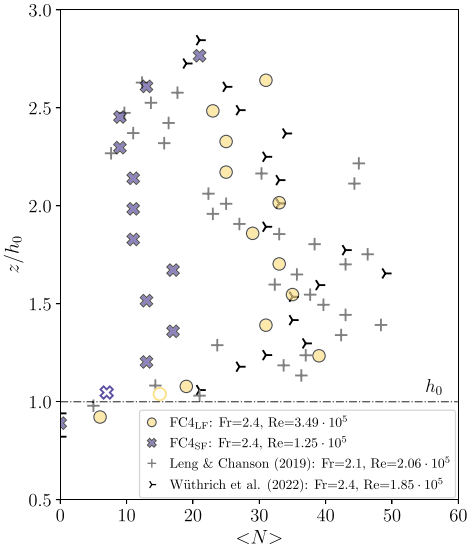

Fig. 11. Comparison of $\langle N \rangle$ for FC4 (Fr = 2.4) at both scales, with data of breaking bore studies by Wüthrich et al. [28], and Leng and Chanson [20] at normalized elevations z/h_0 (note that for breaking bores Fr=$(V_1 + U)/\sqrt{gh_0}$, where V_1 is the velocity of the initial flow). The reference probe measurements (based on 220 tests) are indicated by empty markers.

breaking bores at similar Froude numbers (Fr ≈ 2.4) is likely attributed to differences in inflow conditions. Fig. 11 specifically compares the vertical distribution of $\langle N \rangle$ for FC4 at both scales with the breaking bore data of [20,28], presented as a function of z/h_0. Despite their lower Reynolds numbers compared to FC4$_{LF}$, both breaking bores exhibited higher values of $\langle N \rangle$ in the lower shear layer. This indicates that the number of bubbles is sensitive to turbulence-related processes, influenced not only by variations in Re, but also by the levels of turbulence in the inflow. This is consistent with findings by Montano and Felder [48] who demonstrated that hydraulic jumps with fully developed upstream boundary layers exhibit higher bubble count rates.

The bubble pseudo-chord length L_{ch} (defined by Eq. (1)) provides an estimate of the individual bubble size in the longitudinal direction. Fig. 12 shows the distributions of normalized pseudo-chord lengths, L_{ch}/h_0, for all FCs at three selected elevations, comparing both scales. For all FCs, the small-flume distributions are consistently broader than those in the large flume, indicating the presence of relatively larger bubbles and highlighting noticeable scale effects on bubble size. Comparable scale effects on bubble chord time were observed in steady flows, where lower Reynolds numbers at similar Froude numbers resulted in relatively larger bubbles [12,13].

Comparing dam-break waves at both scales, higher h_0 and Re in the large flume resulted in larger fluctuations in dimensional form (Section 5). This enhances air entrainment, leading to higher bubble counts for FC1$_{LF}$ to FC4$_{LF}$ (Fig. 10). Moreover, in the small flume, lower Reynolds numbers contribute to reducing the turbulent energy dissipation and limiting the range of active turbulent length scales. Bubble breakup is affected by the balance between turbulent stresses and surface tension, with the smallest stable bubble size commonly characterized by the Hinze scale [49] defined as:

$$d_H \sim \left(\frac{We_c \sigma_s}{\rho}\right)^{3/5} \varepsilon^{-2/5}, \tag{4}$$

where We_c is the critical Weber number at bubble level, and ε the turbulent kinetic energy dissipation rate. The reduced dissipation rate ε in the small flume increases d_H, limiting the formation of small bubbles. In addition, lower Reynolds numbers increase the Kolmogorov length scale, reducing the presence of small eddies capable of fragmenting entrained air [50,51]. Altogether, these mechanisms inhibit bubble breakup as capillary forces become relatively more important in the small flume, explaining the observation of fewer but larger bubbles at the smaller scale.

A comparison of FCs at each scale shows that increasing Fr in dam-break waves introduces contrasting effects. Higher Fr correspond to more energetic roller dynamics, resulting in stronger free-surface instabilities and larger velocity gradients. These conditions enhance initial air entrainment at the roller toe and shear-induced breakup within the roller, leading to higher bubble counts at large Fr, particularly within the shear layer. Conversely, in dam-break waves a higher Fr corresponds to a lower Re, affecting the Hinze scale and the range of active turbulent length scales. Comparing $\langle N \rangle$ and L_{ch}/h_0 between FCs shows that FC1$_{LF}$ exhibits a greater number of bubbles that are also relatively larger than those in FC4$_{LF}$ (Figs. 10b, 12a,d). This suggests that, in the large flume, turbulent dissipation rates may be sufficiently high to enhance fragmentation, while the smallest stable bubble size remains constrained by d_H, which is relatively larger for FC1$_{LF}$.

In contrast, increasing Fr at the smaller scale does not lead to a substantial rise in the local maximum number of interfaces (Fig. 10b). Although higher Fr may enhance air entrainment and shear, the Reynolds numbers in the small flume flow appear too low for inertial effects to dominate. Consequently, turbulent energy dissipation

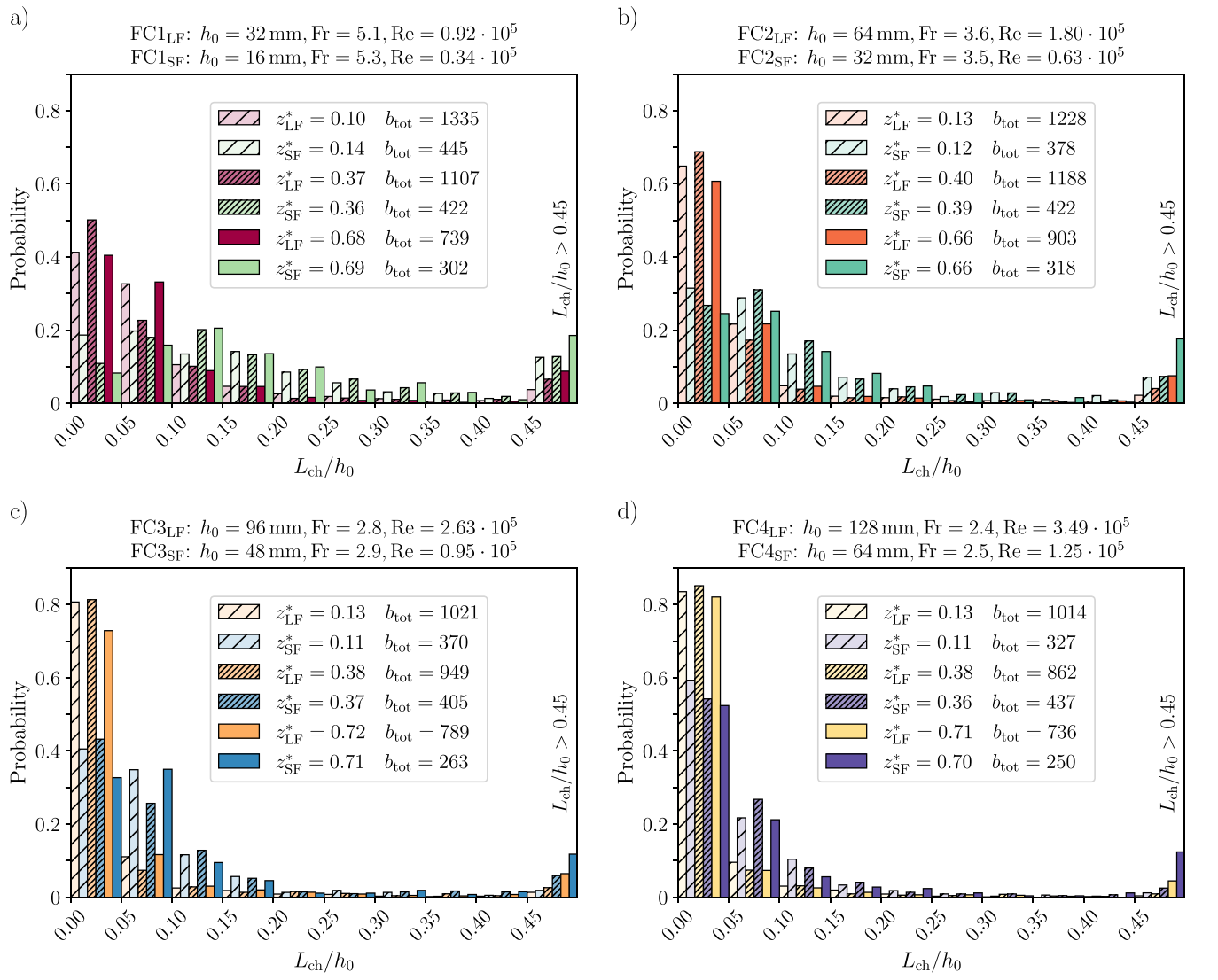

Fig. 12. Comparison of probability distributions of the normalized pseudo-chord length L_{ch}/h_0 at 3 selected elevations z^* for flow conditions FC1–FC4 (Fr = 2.4–5.2) at both scales. Distributions are based on the total (cumulative) number of bubbles b_{tot} recorded over 55 repetitions at each elevation.

rate may be insufficient to reduce the Hinze scale below characteristic bubble sizes and enable effective fragmentation, resulting in relatively constant number of interfaces across the different FCs at small scale.

The contrast between FCs across both scales highlights the reduced sensitivity of small-scale dam-break waves to Froude-driven effects and underscores the dominant role of Reynolds-dependent turbulence. Overall, the observed variations in bubble characteristics across flow conditions and scales reflect the complex interplay of multiphase flow processes and associated scaling effects.

6.2. Void fraction

The ensemble-averaged void fraction C (defined in Eq. (2)) represents the probability of air presence at a given location and time. Fig. 13 presents contours of C for $FC4_{LF}$, showing the spatial and temporal distribution of aeration along the roller, together with z_{90} (elevation where C=0.9), and the median free-surface elevation obtained from ADM data. As discussed for Fig. 5, the ADM detects slightly lower free-surface elevations than z_{90}, corresponding to $C \approx 0.7 - 0.5$ in the aerated region, then converging toward h_p further downstream. Highest aeration levels occur near the roller toe, with continuous aerated regions extending slightly below the free surface along the roller. Locally increased values of C are observed for $0.08 < z^* < 0.3$, consistent with local maxima in the number of detected interfaces (Fig. 10a), supporting the presence of a shear layer just above the initial water level h_0. Similar trends are observed across all flow conditions and both scales.

Table 2 summarizes analytical models for instantaneous void-fraction profiles in the roller. In unsteady flows near the toe, void fractions can be described by an air-mass conservation model balancing turbulent diffusion and buoyancy-driven detrainment [21]. In steady flows, the profile is commonly represented by two distinct advection–diffusion models for a recirculation zone and a shear layer, separated at elevation z_{shear} [e.g., 15,52,53]. Initially developed for hydraulic jumps, the corresponding void-fraction distributions for the recirculation zone and shear layer are given by Eqs. (6) and (7), with fitted diffusivity coefficients D^* and $D^\#$, respectively, representing local advection–diffusion processes governing air transport [53,54]. Although widely used, this two-layer formulation introduces a discontinuity at z_{shear}, therefore neglecting vertical interactions between the two regions.

A more recent model, originally developed for spillway flows, overcomes this limitation through a continuous formulation in which the flow alternates probabilistically between the shear layer and recirculation zone, while interface fluctuations are represented through the convolution of probability distributions [55,56]. This model, described by Eq. (8), extends the conventional two-layer approach by weighting

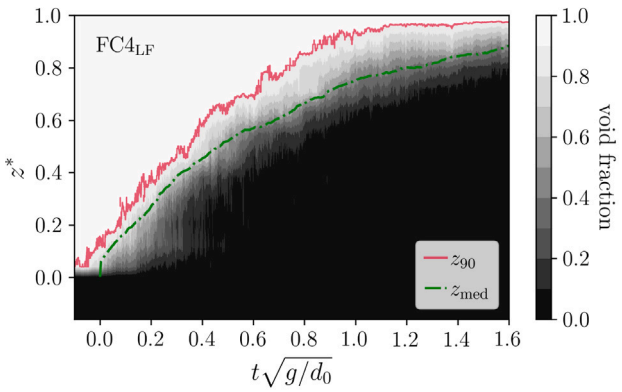

Fig. 13. Contour plot of the ensemble-averaged instantaneous void fraction, C, for $FC4_{LF}$ [Fr = 2.4, Re = 3.49 ·10^5; d_0 = 0.8 m; h_0 = 0.0128 m], with elevation z_{90} corresponding to C=0.9, and the median free-surface elevation z_{med} obtained from the ADMs.

the contributions of Eqs. (7) and (6) with factor Γ, which follows a Gaussian distribution, where z_{shear} represents the mean interface elevation and σ^* its standard deviation, characterizing interface fluctuations [55]. Consequently, an additional parameter is introduced, σ^*, alongside D^* and $D^{\#}$.

For spillway flows, Kramer and Valero [55],Valero and Bung [57], and Kramer [56] showed that the near-surface region is governed by both entrained air and intermittent air entrapment and transport induced by free-surface fluctuations. The resulting upper-region void fraction reflects the superposition of these processes, described by a Gaussian error-function C-profile [57], mathematically equivalent to Eq. (6). In this interpretation, the denominator represents a characteristic thickness of the aerated wavy layer accounting for intermittency, rather than solely diffusive mixing [55–57].

Figs. 14 presents instantaneous void-fraction profiles at four streamwise locations for each FC and scale, compared with analytical models (Table 2) along the roller. To apply models originally developed for steady flows, the temporal evolution in the present data is transformed into spatial evolution using $x = Ut$. For all flow conditions and scales, the vertical distributions exhibit buoyancy-dominated convex profiles immediately downstream of the roller toe, which gradually transition to an S-shape as air bubbles increasingly interact with turbulent flow structures. The S-shaped profiles consist of a lower shear layer and an upper recirculation zone, with local maxima C_{max} within the shear layer increasing with Fr. The shear layer progressively weakens as bubbles break, diffuse and rise under buoyancy, resulting in air being detected only within the recirculation zone further downstream. The measured C-profiles show good agreement with the various analytical models for air–water flows and closely resemble observations reported for breaking bores, spillways, and hydraulic jumps [e.g., 15,28,52,55–58]. The two analytical steady-flow methods show minimal differences; however, the two-state convolution model more accurately captures the vertical transition between flow regimes in the water column. Apart from slight differences in C_{max} within the shear layer, particularly for FC1, the large- and small-flume measurements exhibited comparable downstream evolutions in both magnitude and profile shape. This trend is also reflected in the depth-averaged void fraction C_{mean}, computed by integrating the C-profiles over the roller height (Eq. (3)). Fig. 15a,b present the distributions of C_{mean} along the roller for the large and small flumes, respectively. Comparable FCs exhibit very similar profiles, primarily reflecting a dependence on Fr. The highest values are observed for $FC1_{LF}$ and $FC1_{SF}$, with $C_{mean,max} \approx 0.4$ (Fig. 15c).

The diffusivity coefficients, D^* in Eqs. (6) and (8), and $D^{\#}$ in Eqs. (7) and (8), were obtained as best fits to the experimental data. Their spatial evolution along the roller is shown in Fig. 16 for both

Table 2
Summary of analytical advection-diffusion models.

air diffusion model at the toe of wavefront [21]		
$C(z,t) = 0.9\left(\frac{z-h_0}{z_{90}-h_0}\right)^M$ with $M = \frac{0.9}{C_{mean,z}} - 1$	$0 < z < z_{90}$	(5)
air diffusion model in recirculation zone [54]		
$C_{recirc}(z,t) = \frac{1}{2}\left(1 + \text{erf}\left(\frac{z-z_{50}}{2\sqrt{tD^*}}\right)\right)$	$z_{shear} < z$	(6)
air diffusion model in the shear layer [53]		
$C_{shear}(z,t) = C_{max} \cdot \exp\left(-\frac{(z-z_{c_{max}})^2}{4D^{\#}Uth_0}\right)$	$0 < z < z_{shear}$	(7)
Two-state convolution model [55]		
$C(z,t) = C_{shear}(1-\Gamma) + C_{recirc}\,\Gamma$ with $\Gamma = \frac{1}{2}\left(1 + \text{erf}\left(\frac{z-z_{shear}}{\sqrt{2}\sigma^*}\right)\right)$	$0 < z$	(8)

Notes: $C_{mean,z}$ is the depth-averaged void fraction, integrated from $z = h_0$ to $z = z_{90}$; C_{max} is the local maximum of C in the shear layer, and its corresponding elevation $z_{c_{max}}$; z_{50} is the elevation for which $C = 0.5$; z_{shear} is the elevation which defines the interface between the shear layer to the recirculation zone; $D^{\#}$ and D^* are coefficients in the shear layer and recirculation zone, respectively, obtained from the best-fit analysis of the data; σ^* characterizes the standard deviation of the interface fluctuations, obtained from the best-fit analysis of the data.

steady-flow models. Note that $D^{\#}$ is non-dimensional, whereas D^* is dimensional and normalized by Uh_0. The two analytical methods show only minimal differences in the fitted coefficients for both D^* and $D^{\#}$. For all FC at both scales, the recirculation diffusivity coefficient D^* decreases with increasing distance from the roller toe (Fig. 16a,b). Across scales, the normalized coefficient $D^*/(Uh_0)$ exhibits comparable values, suggesting a stronger dependence on Fr, which is less apparent in dimensional form. For $FC1\text{-}4_{LF}$, the magnitude of D^* decays from approximately 0.015 m^{2}s^{-1} near the roller toe to 0.0001 m^{2}s^{-1} [2], consistent with values reported for breaking bores at Fr = 2.1, Re = 1.85 · 10^5, and Fr = 2.4, Re = 2.3 · 10^5 [21,28]. In contrast, the small-flume experiments yield dimensional values that are almost an order of magnitude lower near the roller toe, i.e. $\mathcal{O}(10^{-3})$. The shear-layer coefficient $D^{\#}$ exhibits greater spatial variability (Fig. 16c,d), reflecting the unsteady nature of the flow and the associated scatter in the fitted data, despite the presence of a clearly identifiable shear layer in all FCs. Nevertheless, $D^{\#}$ shows an increasing trend along the roller before decaying downstream, with values comparable to previous studies of breaking bores, ranging between 0.02 to 0.06 [21]. Similar to the normalized recirculation coefficient, the shear diffusivity remains of the same order of magnitude at both scales and shows a clearer dependence on Fr, with the highest values observed for $FC1_{LF}$ and $FC1_{SF}$. The additional normalized optimization parameter, σ^*/h_0, in the two-state convolution method (Eq. (8)) ranged from 0.01 to 0.9, with slightly larger values observed for higher Froude numbers and for the smaller flume.

The comparable magnitude and shape of the void-fraction distributions at both scales are consistent with previous studies reporting quasi-self-similarity and limited scale dependence [12,17,18,59]. However, differences in inflow conditions and flow properties between steady and unsteady flows may limit this comparison and raise questions regarding the interpretation and applicability of models originally developed for steady flows. In particular, it remains uncertain whether the upper region of the dam-break wave is governed by diffusive mixing analogous to the recirculation zone of a hydraulic jump. Since dam-break waves also feature fluctuating free surfaces and associated (de-)aeration and transport processes, the interpretation based on spillway flows, in which flow processes reflect the combined effects of entrained bubbles and intermittently trapped air, may suitably describe the governing dynamics in the upper region. Both interpretations, however, are based on steady-flow phenomena. The authors therefore emphasize that the good agreement between the dam-break wave

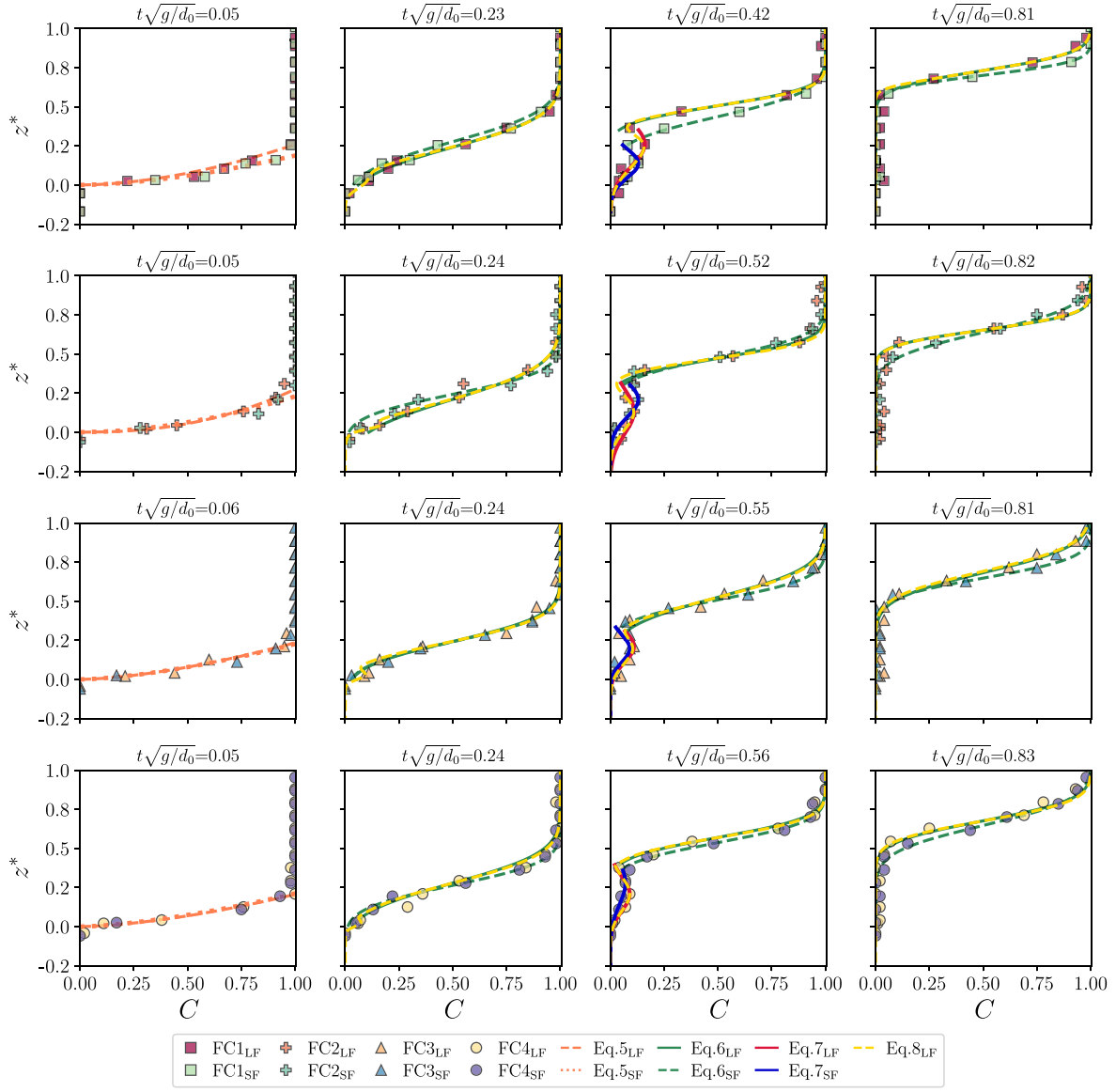

Fig. 14. Comparison of instantaneous void-fraction profiles C as a function of the normalized elevation z^* between the experimental measurements and analytical air-diffusion models (see Table 2) for flow conditions FC1–FC4 across both scales. For clarity, two-state convolution method (Eq. (8)) is shown only for the large-flume measurements, but similar profiles were also observed for the small-flume measurements.

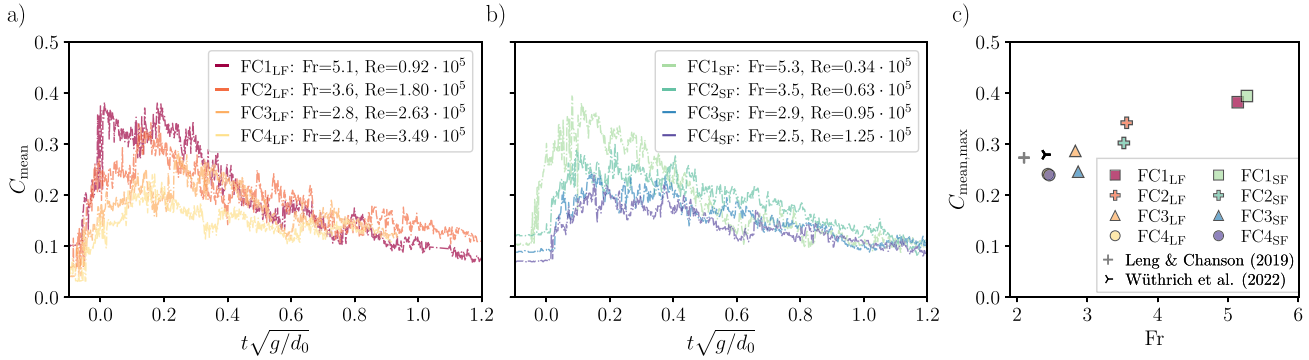

Fig. 15. Depth-averaged void fraction C_{mean}: (a) Comparison of C_{mean} for FC1$_{LF}$-FC4$_{LF}$ at large scale (d_0 = 0.8 m; h_0 = 0.032 - 0.128 m). (b) Comparison of C_{mean} for FC1$_{SF}$-FC4$_{SF}$ at small scale (d_0 = 0.4 m; h_0 = 0.016 - 0.064 m), and (c) comparison of $C_{mean,max}$ plotted against Fr for FC1-FC4 across both scales, together with data from breaking-bore studies by Leng and Chanson [20] [Fr = 2.1, Re = 2.06·10^5] and Wüthrich et al. [28] [Fr = 2.4, Re = 1.86·10^5]. Note that for both previous studies Fr=$(V_1 + U)/\sqrt{gh_0}$, where V_1 is the initial flow velocity.

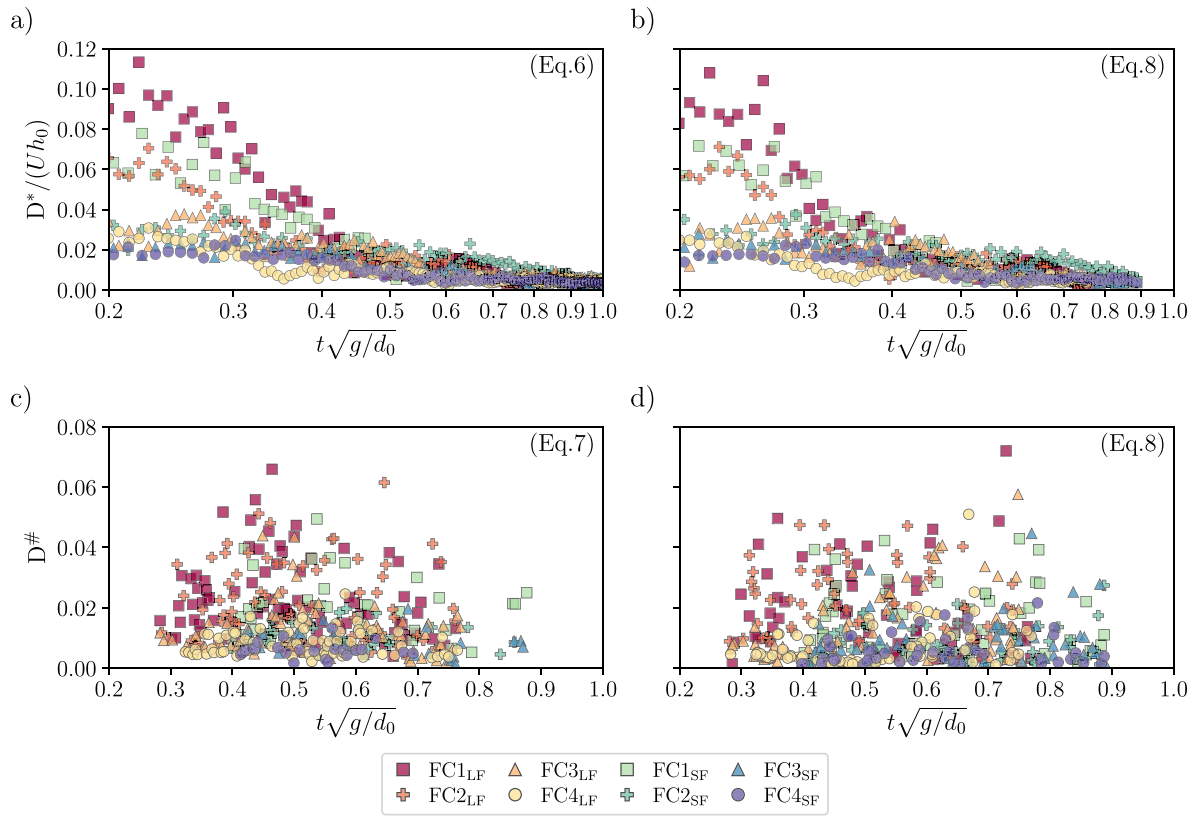

Fig. 16. Comparison of diffusivity coefficients along the roller for flow conditions FC1-FC4 at both scales (LF: d_0=0.8 m, SF: d_0=0.4 m): (a) D^* in the recirculation zone obtained for Eq. (6), (b) D^* in the recirculation zone obtained for Eq. (8), (c) $D^\#$ in the shear layer obtained for Eq. (7), and (d) $D^\#$ in the shear layer obtained for Eq. (8).

measurements and the analytical models does not necessarily imply identical underlying physics. Instead, it indicates that the shape of the void-fraction distributions can be described by the available analytical solutions (Table 2), while the diffusivity coefficients should be interpreted as model parameters rather than direct measures of turbulent diffusivity. At the same time, the void-fraction measurements exhibit only limited variation between scales, suggesting quasi-self-similar behavior and weak scale dependence comparable to trends observed in steady two-phase flows, even if the governing physical mechanisms are not strictly identical.

7. Discussion

This study investigated the multiphase hydrodynamic behavior of dam-break waves in two geometrically proportional flumes. A comprehensive dataset, combining intrusive and non-intrusive measurement techniques across four Froude numbers at each scale, enabled a direct assessment of multi-scale behavior on both free-surface dynamics and air–water flow properties. Despite this, some open questions remains and these are addressed here.

7.1. Scaling of instrumentation

When interpreting the results, it should be noted that the instrumentation, including the conductivity probes and the high-speed video camera, is not geometrically scaled. Each probe tip consists of an inner electrode ($\varnothing$ = 0.25 mm), such that the smallest detectable bubble is constrained by the probe geometry and the minimum bubble size does not scale with the flow. Moreover, top-view recordings in the small flume benefit from a lower camera position, resulting in different spatial resolutions (0.43 mm for the small flume and 0.76 mm for the large flume). Consequently, the small flume videos may capture more small-scale fluctuations per pixel than the large flume, which could contribute to the slightly higher normalized standard deviations of the roller-toe fluctuations observed in the small flume (Fig. 7b).

7.2. Turbulence and energy dissipation processes

Distinct trends emerge when comparing the hydrodynamic behavior of the free surface and the roller toe across scales. Under Froude similitude, normalized free-surface fluctuations scale well at the roller toe, whereas clear scale effects are observed along the wavefront. This contrast is likely attributable to the different physical processes captured by the two metrics: roller-toe fluctuations represent the motion of a kinematic boundary largely governed by global, inertia-dominated flow dynamics. In contrast, free-surface fluctuations along the roller are more strongly influenced by (de-)aeration processes and large coherent structures associated with recirculating mixing beneath the free surface, enhancing sensitivity to scale-dependent effects. Furthermore, Fig. 7b shows slightly larger normalized standard deviations in the small flume than in the large flume for similar Fr. In addition to differences in video spatial resolution, this may be related to varying energy dissipation mechanisms. Although the total available energy is proportionally similar in both setups, the dominant dissipation mechanisms likely differ: in the large flume, a greater fraction of energy may be dissipated through aeration, whereas in the small flume dissipation appears to be governed by slightly stronger (normalized) roller-toe fluctuations.

Overall, the results indicate that bubble number and size are highly scale-dependent: $\langle N\rangle_{max}$ = 52 for FC1$_{LF}$, compared to $\langle N\rangle_{max}$ = 22 for FC1$_{SF}$ (Fig. 10a), while on average ≈75% of the bubbles are smaller than $0.1L_{ch}/h_0$ in FC1$_{LF}$, compared to only ≈30% in FC1$_{SF}$ (Fig. 12a). Section 6.1 discussed the scale dependence of bubble characteristics in relation to turbulence-controlled breakup mechanisms, providing a qualitative physical explanation based on established concepts in the

literature. However, no direct measurements of turbulence intensity or energy dissipation rate are available in the present study to quantitatively substantiate this interpretation, which remains speculative. Quantitative characterizations of turbulence properties in strongly unsteady air–water flows remain a key challenge, and future research is needed to directly relate turbulence dissipation and its role in bubble breakup mechanisms under unsteady flow conditions.

7.3. Steady vs. unsteady conditions

To the author's best knowledge, this is the first study to investigate scaling effects on air–water flow properties of unsteady breaking rollers. Due to the limited availability of unsteady air–water flow data, the results were compared with well-studied steady multiphase flows, particularly hydraulic jumps. Dam-break waves, breaking bores, and hydraulic jumps share key features, including the transition from supercritical to subcritical flow through a turbulent recirculating region accompanied by strong free-surface deformation, energy dissipation, and air entrainment. Consequently, bores and dam-break waves are often, in first approximation, described as "hydraulic jumps in translation" [e.g., 1,60,61], assuming that, in a reference frame moving with the front, the breaking roller resembles that of a stationary hydraulic jump. Their principal flow characteristics are therefore commonly related through the inflow Froude number, formulated here in its general form as $\mathrm{Fr} = (V_1+U)/\sqrt{gh_0}$. Despite these similarities, some differences remain. Hydraulic jumps are stationary (i.e., $U = 0$), whereas bores and dam-break waves are transient and time-dependent. In addition, dam-break waves propagate over still water (i.e., $V_1 = 0$), unlike hydraulic jumps and bores, which develop against an upstream current. Consequently, bores and hydraulic jumps contain a (partially) developed inflow boundary layer and pre-existing turbulence, whereas dam-break waves do not. Although the present dam-break waves were compared with available bore and hydraulic-jump datasets at similar Fr, differences in generation mechanisms and inflow conditions inherently produced variations in Reynolds number, turbulence levels, inflow velocity, and water depth. These factors likely influence air entrainment, bubble breakup, and transport processes, indicating that similar Froude numbers do not necessarily imply equivalent air–water behavior.

Despite this, the present results showed broad agreement with previous studies in the observed trends of free-surface fluctuations and air–water flow properties. However, several findings also highlighted important distinctions between the different flows. Fig. 11 showed that breaking bores had more bubbles within the shear layer than $\mathrm{FC4_{LF}}$, despite lower Re and similar Fr, reflecting enhanced upstream turbulence associated with the inflow boundary layer. Moreover, although of the same order of magnitude, the shear-layer void-fraction maximum ($C_{\max}$ and $z_{C\max}$) and the modeled parameters (D^* and $D^{\#}$) were generally smaller in dam-break waves (Section 6.2) than those reported for hydraulic jumps [e.g., 13,15,18,52]. These differences suggest that air–water properties are possibly influenced by both the transient nature of dam-break waves and the absence of a developed inflow boundary layer, and further imply that transport processes may differ from the diffusive mixing that characterizes hydraulic jumps. However, these interpretations remain largely qualitative because direct quantitative comparisons between steady and unsteady aerated flows are scarce, pointing out the need for further research. This means that comparing scale effects between steady and unsteady flows remains challenging and falls within a broader ongoing discussion, where additional factors such as temperature, fluid properties, bed roughness, and salinity also affect aeration dynamics and bubble persistence [41,62,63]. Nevertheless, the similarities identified across the different flow types, as presented in this study, can provide useful insight into potentially shared physical processes and observed trends, provided that the underlying assumptions are recognized.

8. Conclusion

The breaking roller in dam-break waves is characterized by intense recirculation and strong air entrainment, for which the multiphase dynamics remain poorly understood. Since laboratory studies are commonly designed under Froude similitude, down-scaled aerated free-surface flows are affected by scale effects, particularly in their air–water characteristics, due to incomplete dynamic similarity.

This study analyzed the multi-scale behavior of unsteady dam-break wave rollers using geometrically similar experiments conducted in two flumes, with four distinct flow conditions examined at each scale. A comprehensive dataset was obtained through a combination of intrusive and non-intrusive measurement techniques, including acoustic displacement measurements, video analysis, and phase-detection probes, enabling detailed characterization of free-surface dynamics and air–water flow properties.

While normalized roller-toe fluctuations collapse well between scales, indicating Froude-similarity, free-surface fluctuations along the roller do not, revealing a dependence on both Froude and Reynolds. These fluctuations are more strongly influenced by (de-)aeration processes and large coherent structures associated with recirculating mixing beneath the free surface, enhancing sensitivity to scale-dependent effects.

Bubble characteristics exhibit pronounced scale effects, in line with literature. At higher Reynolds numbers, up to twice as many bubbles were detected in the shear layer compared to flows with similar Froude numbers but lower Reynolds numbers. Moreover, at higher Re, about 75% of the bubbles fell within the smallest size ranges, compared to only ≈30% at lower Re for Fr=5.2. In contrast, void-fraction profiles are much less sensitive to scale and comparable depth-averaged void-fraction distributions were observed for each FCs, with maximum values ranging from $C \approx 25\%$–40%, suggesting a primary dependence on Froude.

Overall, this study demonstrated that many multiphase flow properties cannot be directly extrapolated solely based on Froude similarity, confirming valuable similarities with trends reported in previous studies mostly focused on steady flows. However, comparison with breaking bores at similar Froude numbers (but lower Reynolds numbers) revealed a notably higher number of bubbles in the shear layer, likely due to differences in inflow conditions. This highlights the limitations of directly comparing scale effects across different flow regimes and emphasizes the need to expand existing datasets and obtain prototype measurements to improve the extrapolation of laboratory-scale results to natural unsteady phenomena.

Notations

b = number of bubbles [-]
b_{tot} = total number of bubbles detected over n repetitions at elevation z [-]
c = instantaneous void fraction [-]
C = ensemble-averaged void fraction [-]
$C_{\max}$ = local maximum of C in the shear layer [-]
C_{mean} = depth averaged void fraction [-]
d_0 = impoundment depth of reservoir [m]
d_{H} = smallest stable bubble size defined by Hinze scale [m]
d_{b} = bubble diameter [m]
D^* = diffusivity coefficient in upper region of the roller, used in Eqs. (6) and (8) [$\mathrm{m^2/s}$]
$D^{\#}$ = diffusivity coefficient in lower region of the roller, used in Eqs. (7) and (8) [-]
Fr = Froude number, defined as $\mathrm{Fr}= U/\sqrt{gh_0}$ [-]
g = gravitational acceleration [$\mathrm{ms^{-2}}$]
h_0 = initial still water level downstream of the gate [m]
h_{p} = plateau height after the wavefront [m]
IC = indentation coefficient [-]
k = total number of frames per video [-]

L = roller-toe perimeter length [px]
L_{ch} = pseudo-chord length [m]
L_r = roller length [m]
m = number of consecutive frames used to compute the instantaneous celerity u [-]
Mo = Morton number, defined as $\mathrm{Mo} = \mathrm{We}^3/(\mathrm{Fr}^2\mathrm{Re}^4)$ [-]
n = number of repetitions [-]
N = number of interfaces [-]
pi = pixel intensity [-]
pi_{thres} = pixel intensity threshold for binarization of images [-]
Re = Reynolds number, defined as $\mathrm{Re} = (\rho U h_0)/\mu$ [-]
t = time [s]
t^* = normalized time, defined as $t^* = t\sqrt{g/d_0}$ [-]
t_{ch} = bubble chord time [s]
t_{h_p} = time instance at which plateau height h_p is reached [s]
u = instantaneous roller-toe celerity [ms^{-1}]
u_b = longitudinal velocity fluctuation at the bubble diameter scale [ms^{-1}]
U = wavefront celerity [ms^{-1}]
V = raw probe signal [V]
V_{max} = maximum value of probe signal [V]
V_{min} = minimum value of probe signal [V]
W = flume width [m]
W' = effective flume width in cropped images [px]
We = Weber number, defined as $\mathrm{We} = (\rho h_0 U^2)/\sigma_s$ [-]
We_c = critical Weber number at bubble level, defined as $\mathrm{We}_c = (\rho d_b u_b^2)/\sigma_s$ [-]
x = longitudinal distance along the flume [m]
x' = roller-toe fluctuation in longitudinal direction [m]
y = cross-sectional distance [m]
y^* = normalized cross-sectional distance, defined as $y^* = y/W$ [-]
$y_{p,i}$ = cross-sectional distance of probe i [m]
z = vertical distance [m]
z^* = normalized elevation, defined as $z^* = (z - h_0)/(h_p - h_0)$ [-]
$z_{c_{max}}$ = elevation of C_{max} [m]
z_{shear} = elevation marking the transition from the shear layer to the recirculation zone [m]
z_{vc} = vertical position of the camera [m]
z_{50} = elevation where C=0.5 [m]
z_{70} = elevation where C=0.7 [m]
z_{90} = elevation where C=0.9 [m]
Z_{thres} = threshold for Z-score filter [-]
ε = turbulent kinetic energy dissipation rate [Wkg^{-1}]
ρ = water density, herein $\rho = 1000$ [$\mathrm{kg{\cdot}m^{-3}}$]
μ = dynamic viscosity, herein $\mu = 1.002 \cdot 10^{-3}$ [Pa·s]
σ_s = surface tension, herein σ_s=0.07 [$\mathrm{kg{\cdot}s^{-2}}$]
σ^* = model parameter characterizing the fluctuations of z_{shear}, used in Eq. (8) [m]

Abbreviations

ADM	Acoustic Displacement Meter
FC	Flow Condition
FOV	Field of View
fps	frames per second
HDR	High Dynamic Range
IQR	interquantile range
LF	large flume
SF	small flume
SG	Savitzky–Golay filter

CRediT authorship contribution statement

D. Regout: Writing – original draft, Visualization, Validation, Software, Resources, Methodology, Investigation, Formal analysis, Data curation, Conceptualization. **A. van Niekerk:** Writing – review & editing, Validation, Software, Methodology, Investigation, Formal analysis. **D. Wüthrich:** Writing – review & editing, Validation, Supervision, Resources, Project administration, Methodology, Funding acquisition, Conceptualization.

Declaration of competing interest

The authors declare that they have no known competing financial interests or personal relationships that could have appeared to influence the work reported in this paper.

Acknowledgments

This study was supported by the Dutch Research Council NWO (grant OCENW.XS21.2.045). The authors thank the technical staff of the Hydraulic Laboratory at TU Delft, the Netherlands. Additionally, they acknowledge the support of Mr. Jonas Matsch, formerly an MSc student at TU Dresden, Germany, to the experimental work. Helpful discussions with Prof. S.N. Jonkman and dr. K. Dunne (TU Delft, the Netherlands), Prof. H. Chanson (University of Queensland, Australia), and dr. L. Oyarte Galvez (VU Amsterdam, the Netherlands) are acknowledged.

Data availability

Data will be made available on request.

References

[1] H. Chanson, Hydraulics of Open Channel Flow: An Introduction, second ed., Butterworth-Heinemann, Oxford, United Kingdom, 2004.
[2] D. Regout, S.N. Jonkman, D. Wüthrich, Experimental study of air–water flow properties in the breaking roller of dam-break waves, Int. J. Multiph. Flow 185 (2025) 105119, http://dx.doi.org/10.1016/j.ijmultiphaseflow.2024.105119.
[3] G.N. Bullock, C. Obhrai, D.H. Peregrine, H. Bredmose, Violent breaking wave impacts. Part 1: Results from large-scale regular wave tests on vertical and sloping walls, Coast. Eng. 54 (8) (2007) 602–617, http://dx.doi.org/10.1016/j.coastaleng.2006.12.002.
[4] J. Zuo, T. Xu, D.Z. Zhu, H. Gu, Impact pressure of dam-break waves on a vertical wall with various downstream conditions by an explicit mesh-free method, Ocean Eng. 256 (2022) http://dx.doi.org/10.1016/j.oceaneng.2022.111569.
[5] W.L. Chuang, S.Y. Chen, Laboratory observation of impact pressure, fluid velocity, and air fraction during dam-break impacts on a square prism, Phys. Fluids 37 (7) (2025) http://dx.doi.org/10.1063/5.0273311.
[6] F. Garoosi, A. Nicole Mellado-Cusicahua, M. Shademani, A. Shakibaeinia, Experimental and numerical investigations of dam break flow over dry and wet beds, Int. J. Mech. Sci. 215 (2022) 106946, http://dx.doi.org/10.1016/j.ijmecsci.2021.106946.
[7] Y. Ryu, K.A. Chang, R. Mercier, Application of dam-break flow to green water prediction, Appl. Ocean Res. 29 (3) (2007) 128–136, http://dx.doi.org/10.1016/j.apor.2007.10.002.
[8] S. Yang, W. Yang, C. Zhang, S. Qin, K. Wei, J. Zhang, Experimental and numerical study on the evolution of wave front profile of dam-break waves, Ocean Eng. 247 (2022) http://dx.doi.org/10.1016/j.oceaneng.2022.110681.
[9] V. Heller, Scale effects in physical hydraulic engineering models, J. Hydraul. Res. 49 (3) (2011) 293–306, http://dx.doi.org/10.1080/00221686.2011.578914.
[10] M. Pfister, H. Chanson, Two-phase air-water flows: Scale effects in physical modeling, J. Hydrodyn. 26 (2) (2014) 291–298, http://dx.doi.org/10.1016/S1001-6058(14)60032-9.
[11] H. Chanson, C.A. Gonzalez, Physical modelling and scale effects of air-water flows on stepped spillways, J. Zhejiang Univ.: Sci. 6 A (3) (2005) 243–250, http://dx.doi.org/10.1631/jzus.2005.A0243.
[12] S. Felder, H. Chanson, Scale effects in microscopic air-water flow properties in high-velocity free-surface flows, Exp. Therm. Fluid Sci. 83 (2017) 19–36, http://dx.doi.org/10.1016/j.expthermflusci.2016.12.009.
[13] F. Murzyn, H. Chanson, Experimental assessment of scale effects affecting two-phase flow properties in hydraulic jumps, Exp. Fluids 45 (3) (2008) 513–521, http://dx.doi.org/10.1007/s00348-008-0494-4.

[14] H. Chanson, Y. Chachereau, Scale effects affecting two-phase flow properties in hydraulic jump with small inflow Froude number, Exp. Therm. Fluid Sci. 45 (2013) 234–242, http://dx.doi.org/10.1016/j.expthermflusci.2012.11.014.

[15] H. Wang, Turbulence and Air Entrainment in Hydraulic Jumps (Ph.D. thesis), The University of Queensland, Brisbane, Australia, 2014.

[16] J. Estrella, D. Wüthrich, H. Chanson, Flow patterns, roller characteristics, and air entrainment in weak hydraulic jumps: Does size matter? J. Fluids Eng. 144 (7) (2022) http://dx.doi.org/10.1115/1.4053581.

[17] H. Wang, H. Chanson, Self-similarity and scale effects in physical modelling of hydraulic jump roller dynamics, air entrainment and turbulent scales, Environ. Fluid Mech. 16 (6) (2016) 1087–1110, http://dx.doi.org/10.1007/s10652-016-9466-z.

[18] J. Estrella, D. Wüthrich, H. Chanson, Two-phase air-water flows in hydraulic jumps at low Froude number: Similarity, scale effects and the need for field observations, Exp. Therm. Fluid Sci. 130 (2022) http://dx.doi.org/10.1016/j.expthermflusci.2021.110486.

[19] S. Felder, H. Chanson, Turbulence, dynamic similarity and scale effects in high-velocity free-surface flows above a stepped chute, Exp. Fluids 47 (1) (2009) 1–18, http://dx.doi.org/10.1007/s00348-009-0628-3.

[20] X. Leng, H. Chanson, Air-water interaction and characteristics in breaking bores, Int. J. Multiph. Flow 120 (2019) http://dx.doi.org/10.1016/j.ijmultiphaseflow.2019.103101.

[21] R. Shi, D. Wüthrich, H. Chanson, Air–water properties of unsteady breaking bore part 2: Void fraction and bubble statistics, Int. J. Multiph. Flow 159 (2023) http://dx.doi.org/10.1016/j.ijmultiphaseflow.2022.104337.

[22] H. Chanson, Y.H. Toi, Physical modelling of breaking tidal bores: Comparison with prototype data, J. Hydraul. Res. 53 (2) (2015) 264–273, http://dx.doi.org/10.1080/00221686.2014.989458.

[23] X. Leng, H. Chanson, P. Lubin, Air bubble entrainment in breaking bores: Physical and numerical CFD modelling, in: 7th IAHR International Symposium on Hydraulic Structures, ISHS 2018, Aachen, Germany, 2018, pp. 585–595, http://dx.doi.org/10.15142/T3FS9Q.

[24] D. Wüthrich, H. Chanson, Discussion of 'Air–water flows', J. Hydraul. Res. 63 (3) (2025) 405–409, http://dx.doi.org/10.1080/00221686.2025.2490164.

[25] D. Wüthrich, D. Regout, Air-water flow properties in dam-break waves: a sensitivity analysis, in: Proceedings of the 10th International Symposium on Hydraulic Structures, Zurich, Switzerland, 2024, pp. 166–175, http://dx.doi.org/10.3929/ethz-b-000675959.

[26] G. Lauber, W.H. Hager, Experiments to dambreak wave: Horizontal channel, J. Hydraul. Res. 36 (3) (1998) 291–307, http://dx.doi.org/10.1080/00221689809498620.

[27] M. Pfister, W.H. Hager, History and significance of the morton number in hydraulic engineering, J. Hydraul. Eng. 140 (5) (2014) http://dx.doi.org/10.1061/(asce)hy.1943-7900.0000870.

[28] D. Wüthrich, R. Shi, H. Chanson, Ensemble-statistical approach in the measurement of air-water flow properties in highly unsteady breaking bores, Rev. Sci. Instrum. 93 (5) (2022) http://dx.doi.org/10.1063/5.0077774.

[29] A. Savitzky, M. Golay, Smoothing and differentiation of data by simplified least squares procedures, Anal. Chem. 36 (8) (1964) 1627–1639, http://dx.doi.org/10.1021/ac60214a047.

[30] A. Cartellier, J.L. Achard, Local phase detection probes in fluid/fluid two-phase flows, Rev. Sci. Instrum. 62 (2) (1991) 279–303, http://dx.doi.org/10.1063/1.1142117.

[31] Y. Chachereau, H. Chanson, Free-surface fluctuations and turbulence in hydraulic jumps, Exp. Therm. Fluid Sci. 35 (6) (2011) 896–909, http://dx.doi.org/10.1016/j.expthermflusci.2011.01.009.

[32] S. Felder, H. Chanson, Phase-detection probe measurements in high-velocity free-surface flows including a discussion of key sampling parameters, Exp. Therm. Fluid Sci. 61 (2015) 66–78, http://dx.doi.org/10.1016/j.expthermflusci.2014.10.009.

[33] L. Toombes, Experimental Study of Air-Water Flow Properties on Low-Gradient Stepped Cascades (Ph.D. thesis), The University of Queensland, Brisbane, 2002.

[34] B. Hohermuth, R. Boes, S. Felder, High-velocity air-water flow measurements in a prototype tunnel chute: Scaling of void fraction and interfacial velocity, J. Hydraul. Eng. 147 (11) (2021) http://dx.doi.org/10.3929/ethz-b-000505832.

[35] R. Shi, D. Wüthrich, H. Chanson, Discussion of "performance of intrusive phase-detection probe with large sensor size in air-water flow measurement and application to prototype hydraulic jump study", J. Hydraul. Eng. 149 (11) (2023) http://dx.doi.org/10.1061/jhend8.hyeng-13563.

[36] D. Wüthrich, R. Shi, H. Chanson, Physical study of the 3-dimensional characteristics and free-surface properties of a breaking roller in bores and surges, Exp. Therm. Fluid Sci. 112 (2020) http://dx.doi.org/10.1016/j.expthermflusci.2019.109980.

[37] D. Wüthrich, R. Shi, H. Chanson, Strong free-surface turbulence in breaking bores: A physical study on the free-surface dynamics and air-water interfacial features, J. Fluid Mech. 924 (2021) http://dx.doi.org/10.1017/jfm.2021.614.

[38] M. Brocchini, D.H. Peregrine, The dynamics of strong turbulence at free surfaces. Part 1. Description, J. Fluid Mech. 449 (2001) 225–254, http://dx.doi.org/10.1017/S0022112001006012.

[39] G. Zhang, D. Valero, D.B. Bung, H. Chanson, On the estimation of free-surface turbulence using ultrasonic sensors, Flow Meas. Instrum. 60 (2018) 171–184, http://dx.doi.org/10.1016/j.flowmeasinst.2018.02.009.

[40] F. Murzyn, H. Chanson, Free-surface fluctuations in hydraulic jumps: Experimental observations, Exp. Therm. Fluid Sci. 33 (7) (2009) 1055–1064, http://dx.doi.org/10.1016/j.expthermflusci.2009.06.003.

[41] P. Nielsen, B. Xu, D. Wüthrich, S. Zhang, Friction effects on quasi-steady dam-break wave propagation on horizontal beds, J. Fluid Mech. 939 (2022) http://dx.doi.org/10.1017/jfm.2022.182.

[42] J. Stoker, Water Waves, Interscience (1957).

[43] J. Hu, H. Chanson, Free-surface turbulence in hydraulic jump breaking roller at low inflow Froude number, in: Proceedings of the 24th Australasian Fluid Mechanics Conference, Canberra, Australia, 2024, http://dx.doi.org/10.5281/zenodo.14213308.

[44] W.H. Hager, R. Bremen, N. Kawagoshi, Classical hydraulic jump: length of roller, J. Hydraul. Res. 28 (5) (1990).

[45] G. Zhang, H. Wang, H. Chanson, Turbulence and aeration in hydraulic jumps: Free-surface fluctuation and integral turbulent scale measurements, Environ. Fluid Mech. 13 (2) (2013) 189–204, http://dx.doi.org/10.1007/s10652-012-9254-3.

[46] R. Shi, D. Wüthrich, H. Chanson, Intrusive and Non-intrusive Air-water Flow Measurements in Breaking Jumps at Low Froude Number and Large Reynolds Number, Technical Report, The University of Queensland, Brisbane, Australia, 2021, http://dx.doi.org/10.14264/4a0c07f.

[47] H. Wang, H. Chanson, Experimental study of turbulent fluctuations in hydraulic jumps, J. Hydraul. Eng. 141 (7) (2015) http://dx.doi.org/10.1061/(asce)hy.1943-7900.0001010.

[48] L. Montano, S. Felder, Effect of inflow conditions on the air-water flow properties in hydraulic jumps, in: Proceedings of the 21st Australasian Fluid Mechanics Conference, Adelaide, Australia, 2018, http://dx.doi.org/10.26190/unsworks/27044.

[49] J. Hinze, Fundamentals of the hydrodynamic mechanism of splitting in dispersion processes, AIChE J. 1 (3) (1955) 289–295.

[50] A.N. Kolmogorov, The local structure of turbulence in an incompressible fluid at very high Reynolds numbers, Dokl. Akad. Nauk SSSR 30 (1941) 301–305.

[51] G. Deane, M. Stokes, Scale dependence of bubble creation mechanisms in breaking waves, Nature 418 (2002) 839–844, http://dx.doi.org/10.1038/nature00967.

[52] Y. Chachereau, H. Chanson, Bubbly flow measurements in hydraulic jumps with small inflow Froude numbers, Int. J. Multiph. Flow 37 (6) (2011) 555–564, http://dx.doi.org/10.1016/j.ijmultiphaseflow.2011.03.012.

[53] H. Chanson, Air entrainment in two-dimensional turbulent shear flows with partially developed inflow conditions, Int. J. Multiph. Flow 21 (6) (1995) 1107–1121, http://dx.doi.org/10.1016/0301-9322(95)00048-3.

[54] H. Chanson, Study of air entrainment and aeration devices, J. Hydraul. Res. 27 (3) (1989) 301–319, http://dx.doi.org/10.1080/00221688909499166.

[55] M. Kramer, D. Valero, Linking turbulent waves and bubble diffusion in self-aerated open-channel flows: Two-state air concentration, J. Fluid Mech. 966 (2023) http://dx.doi.org/10.1017/jfm.2023.440.

[56] M. Kramer, Turbulent free-surface in self-aerated flows: superposition of entrapped and entrained air, J. Fluid Mech. 980 (2024) http://dx.doi.org/10.1017/jfm.2023.1038.

[57] D. Valero, D.B. Bung, Development of the interfacial air layer in the non-aerated region of high-velocity spillway flows. Instabilities growth, entrapped air and influence on the self-aeration onset, Int. J. Multiph. Flow 84 (2016) 66–74, http://dx.doi.org/10.1016/j.ijmultiphaseflow.2016.04.012.

[58] F. Murzyn, D. Mouaze, J.R. Chaplin, Optical fibre probe measurements of bubbly flow in hydraulic jumps, Int. J. Multiph. Flow 31 (1) (2005) 141–154, http://dx.doi.org/10.1016/j.ijmultiphaseflow.2004.09.004.

[59] H. Chanson, C. Gualtieri, Similitude and scale effects of air entrainment in hydraulic jumps, J. Hydraul. Res. 46 (1) (2008) 35–44, http://dx.doi.org/10.1080/00221686.2008.9521841.

[60] J. Battjes, R. Labeur, Unsteady Flow in Open Channels, Cambridge University Press, Cambridge, 2017.

[61] F. Henderson, Open Channel Flow, MacMillan, New York, 1966.

[62] W. Asher, L. Karle, B. Higgins, On the differences between bubble-mediated air-water transfer in freshwater and seawater, J. Mar. Res. 55 (5) (1997) 813–845.

[63] M.E. Salter, E.D. Nilsson, A. Butcher, M. Bilde, On the seawater temperature dependence of the sea spray aerosol generated by a continuous plunging jet, J. Geophys. Res. 119 (14) (2014) 9052–9072, http://dx.doi.org/10.1002/2013JD021376.